NASA-CR-198032

PROGRESS REPORT
Grant No. NAGW-3954

PROGRAM ELEMENT: Magnetospheric Physics

TECHNIQUE RESEARCH AREA: Experiments/Plasma-dust interactions

DESCRIPTIVE TITLE OF INVESTIGATION: Charging of Interplanetary Grains

PRINCIPAL INVESTIGATOR: R. A. Baragiola, Professor
University of Virginia
School of Engineering and Applied Science
Engineering Physics, Laboratory for Space Research
Charlottesville, VA 22903-2442
(804) 982-2907
Signature/Date:_____

CO-INVESTIGATOR: R. E. Johnson, John L. Newcomb Professor
University of Virginia
School of Engineering and Applied Science
Engineering Physics, Laboratory for Space Research
Charlottesville, VA 22903-2442

INSTITUTIONAL AUTHORIZATION: D. W. Jennings, Director
Office of Sponsored Programs
University of Virginia
P. O. Box 9003
Charlottesville, VA 22906
(804) 924-4270
Signature/Date_____

PROPOSED DURATION OF PROJECT: Year 2 Funding: 4/1/95 - 3/31/96

SEAS REPORT NO. UVA/528488/MSE95/101
January 1995

(NASA-CR-198032) CHARGING OF INTERPLANETARY GRAINS Progress Report, 1 Apr. 1994 - 31 Mar. 1995 (Virginia Univ.) 70 p

N95-24066

Unclas

G3/90 0044783

Progress report NAGW-3954

The objective of this program is to quantify, by laboratory experiments, the charging of ices and other insulators subject to irradiation with electrons, ions and ultraviolet photons and to model special conditions based on the data. The system and conditions to be studied are those relevant for charging of dust in magnetospheric plasmas. The measurements are supplemented by computer simulations of charging of grains under a variety of conditions.

Our work for this period involved experiments on water ice, improved models of charging of ice grains in Saturn's E-ring, and the construction of apparatus for electron impact studies and measurements of electron energy distributions.

Electron emission and surface potentials of ice under ion bombardment

We studied electron emission and sputtering during irradiation of amorphous water ice at 60 K by H^+, D^+, He^+, Li^+, Be^+, B^+, C^+, N^+, O^+, F^+, and Ne^+ ions in the energy range from 10 to 100 keV. The electron yields where determined with the standard charge-collection method using suitably biased electrodes [1,2] and the sputtering yields with an ultra sensitive quartz-crystal microbalance that can detect the removal of a tenth of a monolayers of water [3].

We found that for constant velocity (5 keV/amu) ions the dependence of the sputtering yields with projectile atomic number Z is proportional to the square of the Z-dependence of the electronic stopping power dE/dx. The electron yields increase sublinearly with dE/dx, contrary to assumptions made so far in the literature, which just applied results for metal targets [4,5]. We explain this sublinear effect by noting that unlike in metals, where electrons are very mobile and can neutralize any excess charge, ionizations produced in insulators like water ice cannot be screened during electron emission, due to the localization of the electrons. This means that the ionization track produced by each projectile will charge up, transiently, to a potential that will act as a barrier for electron escape. This is a localized charging, that superimposes on any macroscopic charging [6]. Contrary to expectations, this charging of the track is important for the weakly ionizing protons meaning that it will also be important for energetic electrons.

The sputtering studies have shown that the yields are higher than what has been assumed in the past. This has important consequences on estimates of the source of plasma in the inner Saturnian magnetosphere [7].

In another study, supported by NSF but relevant to this work, we found what we term "catastrophic sputtering" for condensed Ar: an increase of the sputtering yield, by up to two orders of magnitude, due to electrical discharges or breakdown produced by irradiation in a weak electric field. So far, we have not found this effect in pure water ice under normal conditions but we cannot rule it out for films thicker than the ion range, for other insulators, or for high environmental electric fields.

New experimental setup for electron irradiations

We obtained a Perkin-Elmer Auger spectrometer which we are adapting to this work, having built already the alignment and support hardware and a differential pumping chamber to connect it to our 60 kV ion accelerator. With this system, we will be able to irradiate insulators with low energy electrons and keV ions and measure the energy distribution of the ejected electrons.

Modeling the charging of ice grains

This year, we modified our previous modeling of charging of micron sized ice grains, for application to Saturn's E-ring. We took into account two aspects ignored in previous studies, which we found to be essential for grains in low temperature plasmas: electron reflection and the threshold in secondary electron emission due to the band gap of the insulator. We calculated the electrical potential of the grain from the balance between different fluxes of charged particles, their energy distribution, and the secondary emission properties of ice. Since the energy distributions and fluxes of incoming and outgoing particles are affected by the potential of the grain, the problem of dynamical charging is a complex one that needed to be treated self-consistently. We found that existing charging models cannot be simply extrapolated to the low energies (<30 eV) common in planetary magnetospheres. Using parameters from the Voyager PLS experiment, we calculated the potential of Saturn's E-ring grains to vary from -5.5V to +5V at distances from 4 to 10 Saturn radii.

Work for the second year

The plan for the next year is to: 1) extend the results obtained using ions on water ice to other ices (CO_2, CH_4, NH_3, etc.), 2) finish installation of the electron irradiation chamber and do the first experiments on secondary electron emission and energy distributions; 3) determine composition changes induced by bombardment and how they affect electron emission and sputtering properties of the ices.

We will finish the installation of the new chamber for electron and ion bombardment. This involves: a) Constructing and installing cooled target stage with temperature control in the range 20 K - 200 K; b) A gas manifold and gas-doser using a micro-capillary array, to grow uniform ice layers; c) Installing electronics and adapting the required software for data acquisition. d) building and installing electronics for use with pulsed projectile beams, to measure both the electron yields and the charging of the target.

The first experiments will measure secondary electron yields. We will study the dependence on film thickness. amd focus on trying to achieve electron energies below 30 eV, which our modeling has show to be those which determine the grain potential in the E-ring environment.

The measurements will also be done as a function of irradiation dose, since insulators typically decompose under impact of ionizing radiation [8]. This decomposition may be accompanied by the loss of different components, at rates that depend on target temperature and which we can monitor by mass spectrometry, as shown in our recent work on ice using Lyman-α radiation [9].

In other materials like methane, irradiation leads to the formation of less volatile compounds, as we have recently verified in our laboratory. To understand these processes, we will look at irradiation induced changes in the solid using photoelectron spectroscopy, by adding cooling capabilities to our Perkin-Elmer 560 ESCA surface analysis system. We will correlate *in-situ* measurements of composition changes induced by bombardment, and changes in electron emission properties.

Computer simulations

Our modeling has shown to be very valuable in establishing the conditions most important for charging and thus guide future experiments. We will start simulating the effect of grain size and topography by using Monte-Carlo simulations of electron emission in different parts of the grain which results when it is traversed by a fast projectile [10]. This work will form the foundation of subsequent simulations that will address the complexities of varying surface compositions within a given grain, different grain shapes, thickness of ice mantles, etc.

List of papers in the last year

R. A. Baragiola, *Ion Induced Kinetic and Auger Electron Emission from Solids*, in *Low Energy Ion-Surface Interactions*, ed. by J. W. Rabalais (1994)

Particle Emission Induced by Ionization Tracks in Water Ice, M. Shi, D. E. Grosjean, J. Schou, and R. A. Baragiola, Nucl. Instr. Meth. (in press)

Charging of Dust Particles by Planetary Plasmas: Application to Saturn's E-Ring, S. Jurac, R. E. Johnson, R. A. Baragiola and E. C. Sittler, submitted to J. Geophys. Res.

References

1) L. N. Dobretsov and M. V. Gomoyunova, Emission Electronics (Israel Prog. Sci. Trans., 1971)
2) R. A. Baragiola, E. Alonso and A. Oliva Florio; Phys. Rev. B19, 121 (1979)
3) N. J. Sack and R. A. Baragiola, Phys. Rev. B (in press)
4) R. A. Baragiola, Nucl. Instr. Meth. B78 (1993) 223
5) R. A. Baragiola, Ion Induced Kinetic and Auger Electron Emission from Solids, in Low Energy Ion-Surface Interactions, ed. by J. W. Rabalais (1994)
6) E. C. Whipple, Rep. Prog. Phys. 44, 1197 (1981)
7) R. E. Johnson, D. E. Grosjean, S. Jurac and R. A. Baragiola, EOS 74, 569 (1993)
8) R.E. Johnson and J. Schou, Mat. Fys. Medd. Dan. Vid. Selsk. 43 (1993) 403.
9) M. S. Westley, R. A. Baragiola, R. E. Johnson, and G. Baratta, Nature (in press)
10) R. Vidal, J. Ferrón and R. A. Baragiola, to be published

Charging of Ice Grains by Low Energy Plasmas: Application to Saturn's E-Ring

S. JURAC, R. A. BARAGIOLA, R. E. JOHNSON

Laboratory for Space Research, Engineering Physics, University of Virginia, Charlottesville, Virginia, 22903

E. C. SITTLER, Jr.

Laboratory for Extraterrestrial Physics, NASA Goddard Space Flight Center, Greenbelt, Maryland, 20771

January 6, 1995

Abstract

The charging of ice grains in planetary plasmas is studied, including the effects of secondary electron emission and backscattering of the incident electrons. It is shown that existing charging models can not be simply extrapolated to the low energy electron regime (below 30 eV) common in planetary magne-

tospheric plasmas. We derive expressions for the electrical potential of a grain immersed in a low energy plasma which more carefully account for electron reflection and the threshold for secondary electron emission. Using plasma parameters from Voyager PLS experiment, we calculate the potential of Saturn's E-ring grains to vary from -5.5 V at 4 R_s to 5 V at 10 R_s.

1. INTRODUCTION

The E-ring is a diffuse, azimuthally symmetric distribution of small water-ice grains in Saturn's magnetosphere occupying the region between 3 and 8 Saturnian radii. This ring appears to be composed predominantly of ice grains (1 ± 0.3 micrometer in radius, *Showalter et al.*, 1991), which are surrounded by a low-density plasma consisting of electrons, protons and single-ionized oxygen ions (*Richardson and Sittler,* 1990). Three spacecraft have traversed Saturn's magnetosphere and measured plasma parameters: Pioneer 11, Voyager 1 and Voyager 2. The availability of spacecraft measurements makes the E-ring grains excellent candidates for testing aspects of the charging of small grains in a space-plasma environments. This is especially relevant since in the near future the Cassini spacecraft will make many passes through the E-ring region measuring the plasma energy and composition and the dust particle masses and velocities.

The potential of the E-ring grains has been estimated and used as a parameter in recently proposed models for evolution of the E-ring particles by *Horanyi et al.*

(1992), *Morfill et al.* (1993) and *Hamilton and Burns* (1994). *Horanyi et al.* (1992) calculated the motion of the grains launched from Enceladus (a moon of Saturn which is the presumed source of the E-ring material) in the presence of a gravity field, solar radiation pressure, and electromagnetic forces. They showed that micron-sized grains, which are launched over a period of time and which obtain potentials between -5.4 and -5.8 V, would give a grain size and spatial distribution with many of the characteristics of the observed E-ring. *Morfill et al.* (1993) calculated the effect of grain potential on the sputtering rate of the E-ring grains. They suggested that the surrounding plasma is produced and maintained by "self-sputtering"of the E-ring. That is, the sputtered atoms and molecules are ionized and "picked up" by a planetary magnetic field and accelerated to corotation energies. These ions then bombard the dust resulting in a self-sustained process. Since the secondary electron emission coefficients, which play a crucial role in the grain charging, were not known for water ice, each of these groups of researchers made a parameter study of the effect of interest using a "best guess" for the secondary electron yield and the grain potential. In describing grain erosion *Morfill et al.* (1993) used a maximum yield, $\delta_m \approx 1$, at energy $E_m \approx 1000$ eV for the secondary electron emission parameters for energetic electrons incident on water-ice. Applying the grain-charging model described by *Draine and Salpeter* (1979) this gave E-ring grain potentials varying from -40 V at a distance 5 R_s from Saturn to 1 V at 9 R_s from Saturn, where R_s is the radius of Saturn. *Horanyi et al.* (1992) used

the procedure described by *Whipple* (1981) and three values of δ_m with $E_m = 500$ eV. They estimated grain potential at the orbit of Enceladus ($\sim$4 R_s) between -8 and -4 V. In the orbit calculations they favored $\delta_m = 1.5$ which gives the grain potentials varying from -6 V (at 4 R_s) to +3 V (at 8 R_s). *Hamilton and Burns* (1994) calculated the motion of charged grains in the presence of gravitational forces, Lorentz forces, and solar radiation pressure using -5 V as the grain potential near Enceladus orbit. They found for this particular potential that the E-ring could sustain itself; i.e., charged grains comprising the E-ring strike Enceladus at high velocity ejecting new material.

Using laboratory data for secondary electron yields (*Matskevich and Mikhailova,* 1960) we recalculate values of the E-ring grain potential. We will show that extrapolation procedures for obtaining a grain potential used previously can not be done for the low energy plasmas in the Saturnian and other planetary magnetospheres, having electron temperatures usually lower than $\sim$ 30 eV. For low energy plasmas, not only "true" secondary emitted electrons but also "reflected" electrons (a distinction based on their respective energies) constitute emitted currents from the grain and significantly influence its equilibrium electrical potential. In addition, the threshold energy for secondary electron emission, determined by the binding energy of the valence electrons, should be taken into account whenever a significant portion of the electron plasma is below this threshold energy: i. e., does not produce secondary

electrons. In section 2 we review the charging mechanism for a single-grain model surrounded by a plasma with Maxwellian energy distribution commonly used to calculate grain potentials. We emphasize problems that occur when models derived for high energy plasmas (hundreds of eV and higher) are extrapolated to the low energy regime. In section 3 we discuss secondary electron emission and derive the relation for the secondary electron current appropriate for small incident energies. In section 4 we discuss the importance of the reflection coefficient for elastically and inelastically reflected primary electrons, especially for low energy (cold) electrons below 20 eV. We then obtain the charging contribution due to the reflected current and apply the results to Saturn's E-ring examining the relative importance of the contibutions to the charging current to find equilibrium grain potentials. The plasma parameters based on the Voyager measurements are given in section 5. Results with applications to the other existing E-ring evolution models are given in section 6 and 7.

2. CHARGING MECHANISM

The potential of a grain depends on the energy distribution of the surrounding plasma as well as on the properties of the grain itself and it is determined by a balance between various charging currents. Assuming that the main charging mechanism comes from the fluxes of the incoming electrons and ions, the equilibrium potential of the grain is obtained from the current balance equation

$$J_i - J_e + J_{sec} + J_{ref} + J_{h\nu} = 0 \tag{1}$$

where J_e and J_i are electron and ion fluxes incident on a grain, J_{sec} is the escaping flux of secondary electrons, J_{ref} the outgoing flux of reflected primary electrons and $J_{h\nu}$ the photo electron current. Distinction betwen secondary emitted electrons and reflected primary electrons used for calculating the grain potential has been made based on electron energy measurements as will be discussed. The secondary electron energy distribution shows a peak around $E_{sec} = 3$ eV almost independent of the incident electron energy, while a peak which occurs around the incident electron energy is attributed to elastically reflected electrons.

The secondary electron current induced by the electron impact usually determines the charging of a grain. Assuming spherical grains immersed in a plasma with Debye screening length much larger than the grain's radius and that the fluxes of incoming and escaping particles are orbital-motion limited (*Laframboise and Parker,* 1973), the incoming fluxes of electrons (e) and ions (i) have the form

$$J_{e,i} = \int_{\max(0,\pm e\varphi)}^{\infty} [1 \pm (-\frac{e\varphi}{E})] \frac{dj_{e,i}}{dE} dE \tag{2}$$

where $-$ $(+)$ corresponds to electrons (ions), E is the incident electron (ion) kinetic

energy, φ is the grain's surface potential and the factor $[1 \pm (-\frac{e\varphi}{E})]$ accounts for the change in the geometrical cross-section due to Coulomb attraction and repulsion (*Spitzer,* 1941). Although the electron energy distribution function in the planetary environments is closer to a kappa distribution (*Rosenberg and Mendis,* 1992), it can be reasonably fitted using two Maxwellians (*Sittler et al,* 1983). Consequently, for calculating Saturn's E-ring grain potential we evaluate Eq. (2) using two Maxwellian components for the incident electron current: a thermal ("cold") component with temperature T_c and a suprathermal ("hot") component with temperature T_h.

Using a Maxwellian flux distribution for incident electrons Eqs. (2) yields the well known result

$$J_e = \begin{Bmatrix} J_0 \exp(\frac{e\varphi}{kT_e}) \\ J_0 \, (1 + \frac{e\varphi}{kT_e}) \end{Bmatrix} for \begin{Bmatrix} \varphi \leq 0 \\ \varphi \geq 0 \end{Bmatrix} \tag{3}$$

with

$$J_0 = \frac{1}{4} \, n_e \, \overline{v}_e \, , \qquad \overline{v}_e = \sqrt{\frac{8 \, k \, T_e}{\pi \, m_e}} \tag{4}$$

where $n_{e,i}$ is the electron or ion density and $\overline{v}_{e,i}$ is the average thermal velocity.

For bodies with $\varphi < 0$ the secondary emitted flux is obtained based on Eq. (2) as:

$$J_{\mathrm{sec}(\varphi<0)} = \int_{-e\varphi}^{\infty} (1 + \frac{e\varphi}{E}) \, \frac{dj_e}{dE} \, \delta(E + e\varphi) \, dE \tag{5}$$

where $\delta(E)$ is the secondary electron yield. On the other hand, when $\varphi > 0$ not all secondary electrons will escape. Assuming that the velocity distribution of secondary electrons can be approximated by a Maxwellian with peak energies $E_{sec} = kT_{sec}$ (2 - 5 eV), regardless of the form of the incident velocity distribution, *Prokopenko and Laframboise* (1980) found that the escaping secondary electron flux is

$$J_{sec(\varphi>0)} = (1 + \frac{e\varphi}{kT_{sec}}) \exp(-\frac{e\varphi}{kT_{sec}}) \int_0^\infty (1 + \frac{e\varphi}{E}) \frac{dj_e}{dE} \delta(E + e\varphi)\, dE \qquad (6)$$

where the factor $(1 + \frac{e\varphi}{kT_{sec}}) \exp(-\frac{e\varphi}{kT_{sec}})$ in front of the integral represents the fraction of the total electron flux emitted from the grain surface which is able to overcome the grain's potential.

While this charging scheme works for incident electron energies of the order of hundreds of eV, it is not appropriate when energies approach tens of eV. First, at low incident energies, elastic and inelastic reflection becomes the dominant process governing the electron loss from a grain. Also, secondary electron emission starts at some threshold energy (usually between 5 and 10 eV for insulators), not at zero energy which is often assumed in relations for the secondary electron yield $\delta(E)$ derived from the measurements at higher energies. Finally, in the low energy regime the escaping electron flux cannot be approximated by a Maxwellian independent of the incident electron energy because that assumption implies that for small incident energies a

significant portion of the secondary electrons escape with energies greater that the incident energy. Therefore the charging calculation needs to be modified, when the electron temperature is tens of eV or less.

Secondary electron ejection can also be induced by ion or photon impact. The measured ion fluxes are substantially smaller than the electron fluxes and the ion current contribution to the charging is much smaller than the electron contribution. In addition, the ion induced secondary electron yield below 1 keV is small, so the secondary electron current induced by ion impact can generally be ignored. The secondary electron yield is expected to be smaller than 0.1 for ion energies in the order of a hundred eV (*Whipple*, 1981). Therefore, the main contribution to charging is the direct ion current.

For a non stationary grain Eq. (2) should be modified if the grain velocity is comparable to the plasma velocity (*Whipple,* 1981; *Havens et al.,* 1987). This is the case for ions whose measured velocities in the inner edge of the E-ring are comparable to the grain's Keplerian velocity. For the cold ion current we note that the corotating component of velocity is substantially larger than the thermal velocity and the average ion flux to a grain is roughly

$$J_i \approx (1 - \frac{2\ e\varphi}{m_i(v_i - v_{kep})^2})\frac{n_i}{4}(v_i - v_{kep}) \qquad (7)$$

where v_i is measured corrotating component of ion velocity and v_{kep} is the grain speed. We will show later that the ion current contribution to the total current to a grain is

substantially smaller than the electron contribution.

The photoelectron flux is also low. We use the relation given by (*Wallis and Hassan*, 1983)

$$J_{h\nu} = \frac{3}{4} 10^{14} \frac{\chi}{r_{AU}^2} \exp(-\frac{\max[e\varphi, 0]}{1.3\ eV}) \tag{8}$$

to estimate it with the photoelectric efficiency $\chi = 0.1$ for icy grains and Saturn's distance $r_{AU} = 9.6$.

3. SECONDARY ELECTRON EMISSION

Based on the energy spectra of the emitted electrons, the total electron yield, the mean number of ejected electrons per incident electron, is often written as a sum

$$\sigma = r + \eta + \delta \tag{9}$$

of elastically (r) and inelastically (η) backscattered primaries (sometimes added together as "reflected" primaries $R = r + \eta$) and "true" secondary electrons (δ). For incident electrons with energies in the range where secondary electron emission dominates (for example from approximately 100 eV to few keV for ice, Fig. 2) elastically and inelastically backscattered primaries constitute only a small fraction of the total yield. In that case the total yield, σ, is often approximated by the secondary electron yield, δ. But for small incident energies elastically and inelastically backscattered primaries constitute a dominant fraction of all outgoing electrons and in that case reflected electrons can not be neglected.

The secondary electron yield curve $\delta(E)$ is often described by a "universal" shape characterized by two parameters: the maximum yield δ_m and the energy at which it occurs, E_m. Typically, the maximum electron yield δ_m is greater for insulators and semiconductors (1-10) than for metals (0.5-2). In the energy range where the total electron yield of a material is greater than one, the electron current (like an incoming ion current) contributes to positive charging.

Here we use the empirical relation for the dependence of the secondary electron yield given by *Draine and Salpeter* (1979)

$$\delta(E) = \delta_m \frac{4(\frac{E}{E_m})}{(1+\frac{E}{E_m})^2} \tag{10}$$

This relation approximates the secondary electron yield for normal incidence. Since the grain is surrounded by plasma with isotropic flux distribution an angle averaged yield is needed. Based on expressions given by *Dionne* (1973, 1975), *Katz et al.* (1977) derived an angular dependence based on the range and energy loss rate for penetrating electrons which reads

$$\delta(E, \cos\theta) = 2.54\ \delta_m \left(\frac{E}{E_m}\right) \frac{1 - \exp(-\,Q\,\cos\,\theta\,)}{Q\,\cos\,\theta} \tag{11}$$

where θ is the angle of incidence of the electron and $Q = 2.28\,(E\,/\,E_m)^{1.35}$. This expression gives an approximation for energies below 4 E_m and for an isotropic primary

electron distribution it may be integrated to give an angle averaged yield (*Whipple*, 1981):

$$\delta(E) = 5.08\,\delta_m \left(\frac{E}{E_m}\right) \frac{Q - 1 + \exp(-Q)}{Q^2} \tag{12}$$

3.1. Secondary electron flux for low incident energies

The secondary electron energy distribution emitted from a material is almost independent of the incident energy E for energies above a hundred eV and is often approximated by a Maxwellian with a temperature of about 3 eV (*Prokopenko and Laframboise*, 1980) which is in reasonable agreement with measurements (*Murashov et al.*, 1991). This is done for mathematical convinience and does not imply a thermal origin of secondary electron emmision. For incident energies of the order of tens of eV or less, we assume that it still can be approximated as a Maxwellian with a peak at $E_{\rm sec} = kT_{\rm sec}$, but we require a cut-off at the incident electron energy. Therefore the velocity distribution of the escaping secondary electrons at the surface of a charged grain, with the required cut-off at the incident electron velocity v, is

$$f(v, v_s)_{\rm sec} = c(v)\ \exp(-\frac{m\,v_s^2}{2\,k\,T_{\rm sec}})\ H\,(\sqrt{\frac{2}{m}(\frac{mv^2}{2} + e\varphi)} - v_s) \tag{13}$$

where v_s is the velocity of the emitted secondary electrons at the surface of a grain, H is Heaviside step function and $c(v)$ a normalization constant determined at $\varphi = 0$. For grains at negative potentials all secondary electrons can escape, but for positive grain potentials only those electrons for which $\frac{1}{2}m\,v_s^2 - e\varphi > 0$ can escape. In order to calculate $J_{\rm sec}$ for a positively charged grain, we find the ratio $\Lambda(E,\varphi)$ between escape fluxes from a grain at a potential φ and a noncharged grain ($\varphi = 0$)

$$\Lambda(E,\varphi) = \frac{\int_{[2e\varphi/m]^{1/2}}^{[\frac{2}{m}(\frac{mv^2}{2}+e\varphi)]^{1/2}} f(v,v_s)_{\rm sec}\ \mathbf{v}_s\cdot\mathbf{n}\ \ d^3\mathbf{v}_s}{\int_0^v f(v,v_s)_{\rm sec}\ \mathbf{v}_s\cdot\mathbf{n}\ \ d^3\mathbf{v}_s}$$

$$= \frac{(1+\frac{e\varphi}{kT_{\rm sec}})\exp(-\frac{e\varphi}{kT_{\rm sec}}) - (1+\frac{E+e\varphi}{kT_{\rm sec}})\exp(-\frac{E+e\varphi}{kT_{\rm sec}})}{1-(1+\frac{E+e\varphi}{kT_{\rm sec}})\exp(-\frac{E+e\varphi}{kT_{\rm sec}})}$$

where $\mathbf{v}_s\cdot\mathbf{n}$ is the secondary electron velocity component in the outward normal direction.This ratio represents a fraction of secondary electrons which are able to overcome the grain potential, i. e. escape from a grain. The total secondary electron flux in for $\varphi > 0$ in Eq. (6) becomes

$$J_{\rm sec,(\varphi>0)} = \int_0^\infty \Lambda(E,\varphi)\,(1+\frac{e\varphi}{E})\,\frac{dj_e}{dE}\,\delta(E+e\varphi)\,dE \qquad (14)$$

When the incident energy is substantially larger than the grain potential, the factor $\Lambda(E,\varphi)$ reduces to $(1+\frac{e\varphi}{kT_{\rm sec}})\exp(-\frac{e\varphi}{kT_{\rm sec}})$ which can be pulled in front of the integral so that Eq. (14) becomes equivalent to the result in Eq. (6).

3.2. Secondary electron emission for H_2O - ice

Unfortunately, very few measurements have been made of the secondary electron yield for water-ice, or for other molecular ices of interest in the outer solar system, especially for low incident energies. Therefore, modellers have used different parameters, δ_m and E_m, as well as different energy dependencies, $\delta(E)$, inferred from the yields measured for other materials.

Recently, *Suszcynsky et al.* (1992) measured the secondary electron yield of an H_2O ice film at normal incidence using a scanning electron microscope. Incident electron energies were between 2 - 30 keV, far above the maximum-yield energy E_m. *Suszcynsky et al.* (1992) used the Sternglass universal curve to extrapolate measured values in the low energy range, predicting the secondary electron emission parameters for water-ice of δ_m =6.8 and E_m =142 eV. These authors were apparently unaware of an earlier measurement of the secondary emission yield by *Matskevich and Mikhailova* (1960) for electron energies from 100 - 2500 eV at normal incidence, using a single pulse method.

Both measurements are plotted in Fig. 1 together with the numerical fit to the data using functional dependences given by Eq. (11) with $\theta = 0$ (curve a) and (10) (curve b), for the secondary electron coefficients δ_m =2.35 and E_m =340 eV. The widely used Sternglass furmula (*Meyer-Vernet*, 1982) is also plotted in the same figure (c) for comparison. Above 1 keV the different fitting formulas give significantly different

yields with Eq. (10) giving the best approximation to the measurements. For the low energy portion of the secondary electron yield curve, which is most important in the E-ring, the fitting formulas do not differ greatly, but the data is very different from the "best guesses" of $\delta(E)$ used by *Morfill et al.* (1993) and *Horanyi et al.* (1992) to calculate the grain potential (Fig. 1). We use Eq. (11) and, as a check Eq. (10), both used in recent models (*Morfill et al.* 1993, *Horanyi et al.* 1992) to see how much the calculated grain potential is affected by the different functional relationships for $\delta(E)$.

As the "temperature" of the secondary emitted electrons, we use the peak energy $\sim$3 eV of the secondary-electrons emitted from quartz (which has secondary electron parameters δ_m and E_m similar to mica, glass and water-ice), measured by *Murashov et al.* (1991).

3.3. Threshold energy for secondary electron production

When dealing with low energy electrons inside the solid it is important to notice that only those absorbing sufficient energy from an incoming electron, ion or photon can leave the surface and contribute to the secondary current. The surface barrier for insulators is determined by the electron affinity (E_A) which is the energy difference between the vacuum level and the bottom of the conduction band. Only those electrons for which the component of kinetic energy perpendicular to the surface is

greater than E_A will escape from the material. In addition, electrons from the valence band need to absorb at least the band gap energy, which is 7.8 eV for cubic ice. Since the electron affinity is 0.9 eV, the valence band edge lies about 8.7 eV below the vacuum level for cubic ice (*Baron et al,* 1977) or about 9 eV for amorphous ice (*Williams et al,* 1974). The primary electron also gains ~0.9 eV (electron affinity) when entering material, so we put the threshold energy for secondary electron production at $E_{th} = 8$ eV. In Figure 2 we plot the functions in both Eqs. (10) and (11), starting at $E_{th} = 8\ eV$ which corresponds to replacing E with $E - E_{th}$ and E_m with $E_m - E_{th}$ in Eqs.(10) and (11).

A lower threshold may result for the excitation of electrons in trap states in the band gap with binding energies $\sim 1-2$ eV (*Haas et al,* 1983). If the grain is negatively charged, then, of course, the excess electrons must reside in traps, which are likely to be near the surface. Although these electrons can be more easily removed from the grain, they constitute an extremely small fraction of the electrons involved in determining the current balance. That is, for a 1 micron radius grain at -10 V there are only 5×10^{-5} excess electrons per surface molecule. Therefore, we will use the threshold value given above for all secondary electrons.

3.4. Secondary electron emission for isotropic incidence

The measurements described above were for normal incidence. *Morfill et al.* (1993) used a multiplying factor of 2 for secondary electron yield to account for both the assumed spherical shape of a dust particle and isotropic incidence (*Draine and Salpeter*, 1979). Measurements show [e. g., *Salehi and Flinn*, (1981)] that the enhancement of the secondary electron yield due to isotropic incidence has a different energy dependence and cannot be accounted for by a simple multiplying factor. It was observed that the secondary electron emission increases with incident angle and that the value of E_m shifts toward higher energies, approximately proportional to $(\cos\theta)^{-1}$. The enhancements of the secondary electron yields due to the small particle effect (*Chow et al.*, 1993), which can be significant for a grain size of order 0.1 μm and smaller, can be ignored in the case of the E-ring grains.

First we use Eq. (11) as a fit for the normal incidence yield and find the angle averaged yield from Eq. (12). In Fig. 3 the dash-dot lines represent normal incidence yield from Eq. (11) (lower line) and the corrected yield for isotropic incidence given by Eq. (12) (upper line). As a check we also find an angle averaged yield using Eq. (10) as the normal incidence yield. For this we use angular dependent measurements (*Salehi and Flinn*, 1981) for $V_2O_5 - P_2O_5 - Cs_2O$ glass which has secondary emission parameters close to ice. We numerically integrated those measurements over all incident angles and find an angle averaged yield which we can scale to ice, assuming

that parameters E_m and δ_m for ice and glass in the case of the isotropic incidence are shifted by the same factor from the normal incidence parameters. We plot in Figure 3 as solid lines the normal incidence yield given by Eq. (10) (lower line) and the calculated angle averaged yield based on Eq. (10) (upper line).

4. REFLECTION COEFFICIENT

A typical ejected electron flux distribution, measured by *Harrower* (1956) for tungsten target at the incident electron energies of 10 and 20 eV, is shown in Fig. 4 (solid lines). The first peak at ~ 3 eV corresponds to secondary electrons while the second peak at the incident energy corresponds to the reflected electrons. The maximum is elastic reflection while inelastic reflected electrons, which lose some of their energy in the interaction with the target, correspond to energies below the elastic maximum. To model such flux distributions at other incident electron energies we use two curves: one for the secondary electrons and the other for reflected electrons and calculate these two current contribution ($J_{\rm sec}$ and J_{ref}) independently. The distinction between the inelastically scattered electrons and the secondary electrons is somewhat arbitrary, but both contributions, $J_{\rm sec}$ and J_{ref}, enter into the total charging current as a sum. The outgoing energy only determines whether the electron can escape from a grain's potential well, i. e. how it contributes to the charging.

For negative grain potentials ($\varphi \leq 0$) all emitted electrons can escape regardless

of their energy and the reflected flux in that case can be calculated using Eq. (5), where δ is replaced by $\eta + r = R$, and where we add both elastically and inelastically reflected electrons in the reflection coefficient.

For positive grain potentials only electrons with sufficient energies escape, i.e., all elastically reflected electrons and those inelastically (as same as secondaries) emitted with energies $\frac{1}{2} m v_r^2 > e\varphi$. To see how the energy distribution of reflected electrons influences the current to a grain, and consequently the grain potential, we present a simple model for reflected current from a charged grain. For the sake of simplicity, we approximate all reflected electrons from an uncharged grain with a half-Gaussian velocity distribution up to the elastic peak at incident electron velocity v

$$f_{ref}(v, v_r) = c'(v)\ \exp(-\frac{m\,(v^2 - v_r^2)}{2\,k\,T_{ref}})\ H(v - v_r) \tag{15}$$

where v_r is velocity of the reflected electrons at the surface, T_{ref} measures the spread of the distribution around the elastic peak, while $H(v - v_r)$ introduces the cut-off at the incident electron energy and $c'(v)$ is normalization constant. We also assume that the electrons are reflected from the small surface element isotropically (*Whipple and Parker* 1969, *Whipple* 1981), which means that reflected fluxes measured from the surface normal follows the experimentally known "cosine law". We use the same procedure as that to obtain Eq. (14) for the secondary electron emission flux to estimate reflected electron contribution J_{ref} in Eq. (1). The total reflected flux for

$\varphi > 0$ is

$$J_{ref,(\varphi>0)} = \int_0^\infty [\frac{1 + (\frac{e\varphi}{kT_{ref}} - 1)\exp(-\frac{E}{kT_{ref}}) - \frac{E+e\varphi}{kT_{ref}}}{1 - \exp(-\frac{E+e\varphi}{kT_{ref}}) - \frac{E+e\varphi}{kT_{ref}}}](1 + \frac{e\varphi}{E})\frac{dj_e}{dE} R(E + e\varphi)\, dE. \tag{16}$$

where R is a measured reflection coefficient. The dashed lines in Fig. 4 represent our approximation for the flux distribution which includes secondary electron flux (with peak at $kT_{sec} = 3$ eV) and reflected flux with our choice for $kT_{ref} = 1$ eV. Due to the finite resolution of the energy analyzer the measured energy spreads around the incident energies (10 and 20 eV) are overestimated (*Harrower*, 1956), and, consequently, our choice for the parameter kT_{ref} represents the upper limit for the actual spread around the elastic peak. However, the change in the equilibrium grain potential introduced by this choice does not exceed 0.1 V, which is less than other estimated uncertainties. It can be concluded that when the elastic peak is sharp (which is the case for water ice, *Michaud and Sanche*, 1987b), the shape of the reflected electron energy distribution does not significantly influence the charge balance.

4.1. Electron reflection from H_2O ice

From measurements of the reflection coefficient for various materials at low incident electron energies (*Bronshtein and Novitskii*, 1978; *Nemchenok et al*, 1976; *Khan et*

al, 1963; *Fridrikov and Shul'man,* 1959) it is known that the reflection coefficient approaches zero as $E \rightarrow 0$, reaches a maximum below ~20 eV, and decreases slowly at higher energies. Typically, for metals the maximum value reaches 0.1 - 0.4, whereas for dielectrics it attains 0.5 - 0.8 (*Dobretsov and Gomoyunova,* 1971).

Measurements of the elastic electron reflectivity of amorphous films of water-ice have been done by *Michaud and Sanche* (1987a, 1987b) for various thicknesses (1-40 monolayers) and for incident electron energies from 1 to 20 eV at 14^0 incidence. Using the same experimental arrangement as *Michaud and Sanche* (1987a, 1987b), *Bader et al.* (1988) measured transmitted current on a 50-layer H_2O film for incident electron energies from 0.1 to 4 eV. *Matskevich and Mikhailova* (1960) measured reflection coefficients for ice in the energy range from 100 eV to 2.5 keV. In Figure 2 we show both measurements together with a least squares fit to the measurements (dashed line) using, for convenience, a form similar to that in Eq. (10), which we use as $R(E)$ in calculations. This fit should be considered only as a rough approximation to the actual functional dependence $R(E)$ in the range of interest, below 1 keV.

5. PLASMA PARAMETERS

For equatorial plasma parameters around Saturn's E-ring we use the model given by *Richardson and Sittler* (1990), which is based on Voyager measurements. The electron energy distribution is fitted by two Maxwellian distributions: thermal ("cold")

component with temperature T_c and suprathermal ("hot") component with temperature T_h. The high energy tail is not well fit using two Maxwellians, but it does not play an important role in our calculation, since the electron fluxes and the secondary electron yields are low in this region. For the proton and oxygen ion densities, we use values extrapolated to the equatorial plane using the Richardson-Sittler model (1990). A Summary of the plasma parameters used are given in Table 1, where $\mathbf{T}_{ec}$, $\mathbf{T}_{eh}$, $\mathbf{n}_{ec}$, and $\mathbf{n}_{eh}$ represent temperatures and densities of the cold and hot electrons respectively. There are, of course, considerable uncertainties in this model, which involved extrapolation of the measured plasma densities to the equatorial plane, and indeed the plasma parameters probably vary in time somewhat. Both the ion and electron temperatures recorded during the Voyager 1 and 2 traverses vary substantially along the same dipole L-shell. Consequently, the distribution of temperatures and densities can be considered a parameter study for grain charging since the distance from Saturn affects the result only via changes in electron temperature and density. Since Voyager 1 crossed the equatorial plane at L $\simeq$ 6 Saturnian radii, equatorial plasma parameters can be determined there and are also given in Table 1.

6. RESULTS: POTENTIAL OF THE E-RING GRAINS

Using Eqs. (8), (3) and (7) for the photon, electron and ion currents, Eqs. (5), (14) for the secondary electron currents and Eqs. (5), (16) for the reflected current, a grain

potential can be found for which the current balance equation (1) is satisfied. As an example, in Figure 5 we give all currents to a micron-sized ice grain at radial distance $L = 6\ R_s$, incident electron current to a grain, secondary electron current, reflected current, sum of the photon and ion currents for H^+ and O^+ ions and, finally, total current to a grain. Current balance is obtained in this case for the grain potential -2 V. As one can see the combined photoelectron curent and the ion current (due to the small ion velocities) to a grain is substantially smaller than other contributing currents; consequently, the equilibrium potential primarily results from balancing different electron currents.

In Figure 6 we show the calculated potential for a spherical grain as a function of radial distance from Saturn for both relationships used for the secondary electron emission (a, b in Fig. 1 and Fig 2). The resulting potential using Eq. (11) for normal incidence yield (and, consenquently, Eq. (12) for the isotropic yield) gives an average $\sim$ 1 V more negative potential than that based on Eq. (10), since the secondary emission yield in that case rises more rapidly up to E_m (Fig. 3). The potential in Fig. 6 is seen to rise from 4-8 R_s and stays almost constant between 8 and 10 R_s. The potential increases in going from Enceladus (4 R_s) to 8 R_s due to increasing electron temperatures (both hot and cold) and increasing densities of the hot electrons. The almost constant potential near Rhea (8.7 R_s) and further outside arises from the fact that, when the positive potential becomes greater than the secondary electron

temperature, $kT_{sec} = 3$ eV, the number of secondaries (which constitutes the major part of the positive current to the grain) sharply decreases. These results are also compared to the best guess of *Morfill et al.* (1993) and three models from *Horanyi et al.* (1992). Agreement is seen to be best with model H2 in which $\delta_m = 2$. In their calculation of E-ring grain orbits *Horanyi et al.* (1992) used δ_m =1.5 and E_m =500 eV, whereas *Morfill et al.* (1993) used δ_m =1 and E_m =1000 eV to describe E-ring grain erosion. The best fit of the experimental yield is obtained with δ_m =2.35 and E_m =340 eV as shown in Fig. 1.

Previous authors have not separated the reflected current in calculating the charging or in calculating the equilibrium potential, which from Fig. 5 is clearly seen to be important at almost all potentials shown. Not including reflection, the E-ring potential would appear 3–5 V more negative than that calculated throughout the full range of distances. Since there are no measurements of the secondary electron yield or the reflection coefficient for ice for a few eV to tens eV, the estimated reflection coefficient in that range (discussed above and given in Fig. 2) is a source of uncertainty for the calculated grain potential. The threshold energy for secondary electron emission also impacts calculated potential when the plasma temperature is low. For instance, not including the threshold energy for the secondary electron production (we use 8 eV) would give potentials $0.5 - 1$ V more positive than those calculated. Since most of the inelastically reflected electrons from ice at low incident energies

suffer small energy losses, all reflected electrons can be considered as having reflected elastically. The choice, $kT_{ref} = 1$ eV (as opposed to $kT_{ref} = 0$ eV, if all electrons were reflected elastically), introduces a change in the grain potential of the order of 0.1 V. Further uncertainties may result from the effects of irregular shapes and roughness of ice grains, impurities in the ice and radiation induced defects which introduce electron states in the band gap, thereby affecting the yields and threshold energies. Using the Voyager 1 ring plane crossing data only (Table 1) the grain potential at 6 R_S would be +3 V as compared to -2 V for value b in Fig. 6. Therefore, the plasma parameters are the largest uncertainty in this calculation.

7. CONCLUSION

In this paper we calculated the charging of an ice grain in Saturn's magnetosphere where the plasma electron temperatures are low. These calculations were based on extrapolations of the complete set of available secondary electron and reflected electron data, taking into account the physics of the secondary electron yields and electron reflection coefficients. We assumed that the grains are one micron solid water-ice spheres, as suggested by most of the measurements (*Showalter et. al.*, 1991.). However, the calculated potentials are not sensitive to the grain size as long as the grains are not much smaller than $\sim 0.1\ \mu m$ and the secondary electron yield parameters for other materials possibly present in the E-ring probably do not differ significantly from

that of water ice. We show that for low incident electrons energies the calculation of the grain potential requires consideration of electron reflection and of the secondary electron production threshold. In fact, for the potentials calculated here for Saturn's inner magnetosphere, varying from about -5.5 V at 4 R_s to 5 V at 10 R_s, reflection is always important, as it is in the case whenever the electron temperature is $< 20\ eV$ or less. Therefore, the charging calculations developed here can be used when the plasma parameters in Saturn's inner magnetosphere are more firmly established and in calculations for other planetary plasmas environments in which a cold electron component is dominant.

Our calculation of the E-ring grain potential vs. distance from Saturn using the plasma data of Richardson and Sittler (1990), which is an average of Voyager data with ion densities extrapolated to the equatorial plane, is seen to be in rough agreement with curve H2 (Fig. 6) in *Horanyi et al.* (1992) who described the spatial distribution of the E-ring. Therefore, our results appear to support this aspect of the hypothesis of the formation and evolution of the E-ring grains. On the other hand, our results differ significantly from the best guess of *Morfill et al.* (1993) for describing a plasma source by low energy ion sputtering of E-ring grains. However, sputtering of the E-ring grains by keV ions does contribute significantly to the plasma formation near Enceladus (*Johnson et al.*, 1993).

Horanyi et al. (1992) and *Hamilton and Burns* (1994) concluded that the spatial

distribution and grain size characteristics of the E-ring could be understood by grains being launched from Enceladus, becoming charged in the ambient plasma, and orbiting under gravitational and electro-magnetic forces. *Horanyi et al.* (1992) showed that if micron-sized grains launched over a period of time from Enceladus (3.95 R_s) would obtain potentials $\sim$ -5.4 to -5.8 V they would disperse over time producing an optical depth profile with a thickness like that of the actual E-ring. In spite of the fact that their "best guess" estimate of the secondary electron coefficients, made in order to obtain the observed E-ring characteristic, underestimates the secondary electron yield below 1 keV, agreement with our potentials occurs because they also neglected the electron reflection coefficient. *Hamilton and Burns* (1994) found that micron-sized grains charged to -5 V would obtain the required orbital eccentricity to account for the spatial extent of the E-ring. That is, they would cross the orbit of Tethys during their life in Saturn's inner magnetosphere. Such potentials are close to those found here at 4 R_s, but the fact that the potential changes with distance from Enceladus must be considered. Therefore calculations presented here appear to confirm aspects of the E-ring hypothesis, if the plasma parameters used are reasonable. These results can now be used for more detailed determination of the physics of the E-ring.

Acknowledgment

We would like to thank M. Michaud and J. Schou for comments, O. Havnes for helpful information, and support from NASA Plasma Physics Division, Geology and Geophysics Division, Magnetospheric Physics Division, and the NSF Astronomy Division.

REFERENCES

Bader, G., J. Chiasson, L. G. Charon, M. Michaud, G Perlozzo, L. Sanche, Absolute Scattering Probabilities for Subexitation Electrons in Condensed H_2O, *Radiat. Res.*, **114**, 467, 1988.

Baragiola, R. A., Principles and mechanisms of ion induced electron emission, Nuclear Instruments and Methods in *Phys. Res.* **B78**, North-Holland, 1993.

Baron, B., and F. Williams, X-ray photoelectron spectroscopy of amorphous ice, *J. Chem. Phys.*, **64**, 3896, 1976.

Baron, B., D. Hoover, F. Williams, Vacuum ultraviolet photoelectric emission from amorphous ice, *J. Chem. Phys.*, **68** , 1997, 1977.

Bronshtein, I. M., and M. G. Novitskii, Secondary electron emission from silicon bombarded with low-energy primary electrons, *Sov. Phys. Solid State* **20** (8), 1467, August 1978.

Chow, V. W., D. A. Mendis, M. Rosenberg, The role of Grain Size and Particle Velocity Distribution in Secondary Electron Emission in Space Plasmas, *J. Geophys. Res.*, **98**, 19065, 1993.

Dionne, G. F., Effects of secondary electron scattering on secondary emission yield curves, *J. Appl. Phys.*, **44**, 5361, 1973.

Dionne, G. F., Origin of secondary-electron-emission yield-curve parameters, *J. Appl. Phys.*, **46**, 3347, 1975.

Dobretsov, L. N., M. V. Gomoyunova, Emissionnaya elektronika, (Izdatelstvo "Nauka", Moscow, 1966), translated and printed in Jerusalem by Keter Press, 1971.

Draine, B. T., E. E. Salpeter, On the Physics of Dust Grains in Hot Gas, Astrophys. J., **231**, 77, 1979.

Fridrikhov, S. A., and A. R. Shul'man, An investigation of the secondary electron emission by certain dielectrics at low primary

electron energies, *Fizika Tverdogo Tela*, **1**, No. 8, 1259, 1959.

Hachenberg, O., W. Brauer, Secondary Electron Emission from Solids, *Adv. Electron. Electron. Phys.*, **11**, 413, 1959.

Hamilton, D. P., J. A. Burns, Origin of Saturn's E ring: Self Sustained, Naturally, *Science*, **264**, 550, 1994.

Harrower, G. A., Energy Spectra of Secondary Electrons from Mo and W for Low Primary Energies, *Phys. Rev* **104**, 52, 1956.

Haas, P. M., M. Kunst, J. M. Warman, Nanosecond Time-resolved Conductivity Studies of Pulse-Ionized Ice. 1. The Mobility and Trapping of Conduction-Band Electrons in H_2O and D_2O Ice, *J. Phys. Chem.*, **87**, 4089, 1983.

Havens, O., T. W. Hartquist, and W. Pilipp, The effects of dust on the ionization structures and dynamics in magnetized clouds, in "Physical Processes in Interstellar Clouds", G. E. Morfill and M. Scholer (eds.), 389, 1987.

Horanyi, M., J. A. Burns, D. P. Hamilton, The Dynamics of Saturn's E-ring Particles, *Icarus*, **97**, 248, 1992.

Johnson, R. E., Energetic Charged-Particle Interactions with Atmospheres and Surfaces, Springer-Verlag, Berlin, 1990.

Johnson, R. E., D. E. Grosjean, S. Jurac, R. A. Baragiola, Sputtering, Still the Dominant Source of Plasma at Dione?, *Eos,* AGU, Trans., **74,** No. 48, 569, 1993.

Katz, I., D. E. Parks, M. J. Mandell, J. M. Harvey, D. H. Brownell, S. S. Wang, M. Rotenberg, A Three Dimensional Dynamic Study of Electrostatic Charging in Materials, *NASA CR-135256, S-Cubed Rep. SSS-R-77-3367,* NASA, Greenbelt, Md., 1977.

Katz I., M. Mandell, G. Jongeward, The Importance of Accurate Secondary Electron Yields in Modeling Spacecraft Charging, *J. Geophys. Res.*, **91**, 13739, 1986.

Khan, I. H., J. P. Hobson, and R. A. Armstrong, Reflection and Difraction of Slow electrons from Single Crystals of Tungsten, *Phys. Rev.* **129**, No. 4, 1513, 1963.

Laframboise, J. G., L. W. Parker, Probe design for orbit-limited current collection, *Phys. Fluids*, **16**, 629, 1973..

Matskevich, T. L., E. G. Mikhailova, Vtorichnaia elektronnaia emissiia plenok l'da i antratsena, *Fizika Tverdogo Tela*, **2**, 709, 1960.

Mendis, D. A., M. Horanyi, Dust-plasma interactions in the cometary environment, in Cometary Plasma Processes (Geophysical Monograph #61, AGU), Ed. A. Johastone, p17, 1991.

Meyer-Vernet, N., "Flip-flop" of Electric Potential of Dust Grains in Space, *Astron. Astrophys.*, **105**, 98, 1982.

Michaud, M. and L. Sanche, Total cross sections for slow-electron (1-20 eV) scattering in solid H_2O, *Phys. Rev. A*, **36**, 4672, 1987a.

Michaud, M. and L. Sanche, Absolute vibrational excitation cross sections for slow-electron (1-18 eV) scattering in solid H_2O, *Phys. Rev. A*, **36**, 4684, 1987b.

Morfill, G. E., O. Havens, C. K. Goertz, Origin and Maintenance of the Oxygen Torus in Saturn's Magnetosphere, *J. Geophys. Res.*, **98**, 11285, 1993.

Murashov, S. V., V. P. Pronin, A. M. Tyutikov, I. I. Khinich, Fine structure of the spectra of truly secondary electrons in dielectrics, *Sov. Phys. Solid State*, **33**, 1068, 1991.

Nemchenok, R. L., T. N. Pal'ts, and A. P. Tsuranov, Secondary electron emission from gallium arsenide due to low-energy primary electrons and characteristic energy losses, *Sov. Phys. Solid State*, **18**, No. 1, 139, January 1976.

Northrop, T. G., Dusty Plasmas, *Physica Scripta*, **45**, 475, 1992.

Prokopenko, S. M. L., J. G. Laframboise, High-Voltage Differential Charging of Geostationary Spacecraft, *J. Geophys. Res.*, **85**, 4125, 1980.

Richardson, J. D., and E. C. Sittler, Jr., A Plasma Density Model for Saturn Based on Voyager Observations, *J. Geophys. Res.*, **95**, 12019, 1990.

Rosenberg, M., D. A. Mendis, A Note on Dust Grain Charging in Space Plasmas, *J. Geophys. Res.*, **97**, 14773, 1992.

Salehi, M., E. A. Flinn, Dependence of secondary-electron emission from amorphous materials on primary angle of incidence, *J. Appl. Phys.*, **52**, 994, 1981.

Showalter, M. R.,J. N. Cuzzi, S. M. Larson, Structure and particle properties of Saturn's E-ring, *Icarus* **94**, 451, 1991.

Sittler, E. C., Jr., Plasma electron analysis: Voyager plasma science experiment, *NASA Technical Memorandum 85037*, GSFC, Greenbelt, Md., 1983.

Sittler, E. C., Jr., K. W. Ogilvie, and J. D. Scudder, Survey of Low-Energy Plasma Electrons in Saturn's Magnetosphere: Voyager 1 and 2, *J. Geophys. Res.*, **88**, 8847, 1983.

Spitzer, L., Jr., The dynamics of the interstellar medium, *Astrophys. J.*, **93**, 369, 1941.

Suszcynsky, D. M., J. E. Borovsky, C. K. Goertz, Secondary Electron Yields of Solar System Ices, *J. Geophys. Res.*, **97**, 2611, 1992.

Wallis, M. K. and M. H. A. Hassan, Electrodynamics of Submicron Dust in Cometary Corona, *Astron. Astrophys.*, **121**, 10, 1983.

Whipple, E. C., L. W. Parker, Effects of Secondary Electron Emission on Electron Trap Measurements in the Magnetosphere and Solar Wind, *J. Geophys. Res.* **74**, 5763, 1969.

Whipple, E. C., Potentials of surfaces in space, *Rep. Prog. Phys.*, **44**, 1197, 1981.

Whipple, E. C., T. G. Northrop, D. A. Mendis, The Electrostatics of a Dusty Plasma, *J. Geophys. Res.*, **90**, 7405, 1985.

Williams, F., S. P. Varma, S. Millenius, Liquid water as a lone-pair amorphous semiconductor, *J. Chem. Phys.*, **64**, 1549, 1974.

FIGURE CAPTIONS

Figure 1. Secondary electron yield for ice vs. incident electron energy (keV): measured by *Matskevich and Mikhailova* (x's) and *Suszcynsky et al.* (diamonds); functional dependences given by Eq.(11) with $\theta = 0$ (a), Eq.(10) (b) and by the "Sternglass law" $\delta(E) = 7.4\delta_m \frac{E}{E_m} \exp(-2\sqrt{\frac{E}{E_m}})$ (c) with δ_m =2.35 and E_m =340 eV; yields used as the "best guesses" by *Morfill et al. (M)* and *Horanyi et al. (H).*

Figure 2. Measured secondary electron yield given by *Matskevich and Mikhailova* (x's) and fitted yields from Eq. (10) (b) and Eq. (11) with $\theta = 0$ (a), both starting at $E_{th} = 8\ eV$ as the threshold energy. The reflected yield measured by *Bader et al.* (squares) and *Matskevich and Mikhailova* (+'s) is shown together with our fit to the actual functional dependence $R(E) = \frac{103.9\ E^{5.23}}{(1\ +\ 1.93\ E)^{5.66}}$ (dashed line).

Figure 3. Secondary electron yield for ice for normal incidence from Eq. (11) (lower dash-dot line) and the corrected yield for isotropic incidence given by Eq. (12) (upper dash-dot line). Solid lines represent the normal-incidence yield given by Eq. (10) (lower line) and the calculated angle averaged yield based on measurements on

glass (upper line).

Figure 4. Total electron fluxes from tungsten for 10 and 20 eV primary electrons at normal incidence measured by *Harrower* (solid lines) and modeled flux distribution (dashed lines) using velocity distributions in Eq. (13) for secondary electrons and that in Eq. (15) for reflected electrons.

Figure 5. All currents to a micron-sized ice grain at radial distance $L = 6$ Saturnian radii: electron current incident to a grain (I_{el}), secondary electron current (I_{sec}), reflected electron current (I_{ref}), sum of the photoelectron and ion currents for H^+ and O^+ ions ($I_{ion+phot}$), and total current to a grain (I_{tot}). The photoelectron and the ion currents are both small, of the order of 10^{-19} A. Current balance is obtained for the grain potential -2 V.

Figure 6. Calculated grain potential as a function of the radial distance in Saturnian radii. Solid lines show the potential determined in this paper using E_m =340 eV and δ_m =2.35. Two different extrapolations for the secondary electron yield lead to slightly different potentials: line (a) based on Eq. (11) and line (b) based on (10). The dash-dot line represents the potential favored by *Morfill et. al. (1993)* with estimated secondary electron parameters

E_m =1000 eV and δ_m =1. Dashed lines show potentials given by *Horanyi et. al. (1992)* using E_m =500 eV and three different values for the maximum yield: δ_m =0 *(H0)*, δ_m =1 *(H1)*, and δ_m =2 *(H2):* their "best guess", based on the observed E-ring characteristics, is δ_m =1.5.

Table 1. Equatorial Plasma Parameters[1,2]

L	T_{ec}	n_{ec}	T_{eh}	n_{eh}	T_{O+}	n_{O+}	T_{H+}	n_{H+}
4	2.7	90	100	0.2	40	70	12	20
5	3.5	45	120	0.4	80	40	14	3.7
6	5.0	27	150	0.4	100	25	16	2
7	6.8	15	170	0.4	120	15	18	1
8	11	4.5	200	0.4	170	4	20	0.8
9	13.5	2.7	250	0.3	220	2.3	22	0.65
10	17	1.9	300	0.2	260	1.6	24	0.5

Table 1. [1] Plasma parameters from *Richardson and Sittler* (1990): temperatures T (eV) and densities n (cm^{-3}) for electrons ("cold" and "hot") and ions (O^+ and H^+) in equatorial plane versus distance in Saturnian radii L

[2] To indicate uncertainties in plasma parameters we used Voyager 1 measurements (*Sittler et al* ,1983) averaged over a two huor period covering the ring plane crossing between $5 < L < 6.7$. The proper electron density is determined from ion density requiring the charge balance. These parameters are: $T_{ec} = 12.3 \pm 2.9$, $n_{ec} = 24.3 \pm 6.2$, $T_{eh} = 99 \pm 50$, $n_{eh} = 1.0 \pm 0.4$

Figure 1

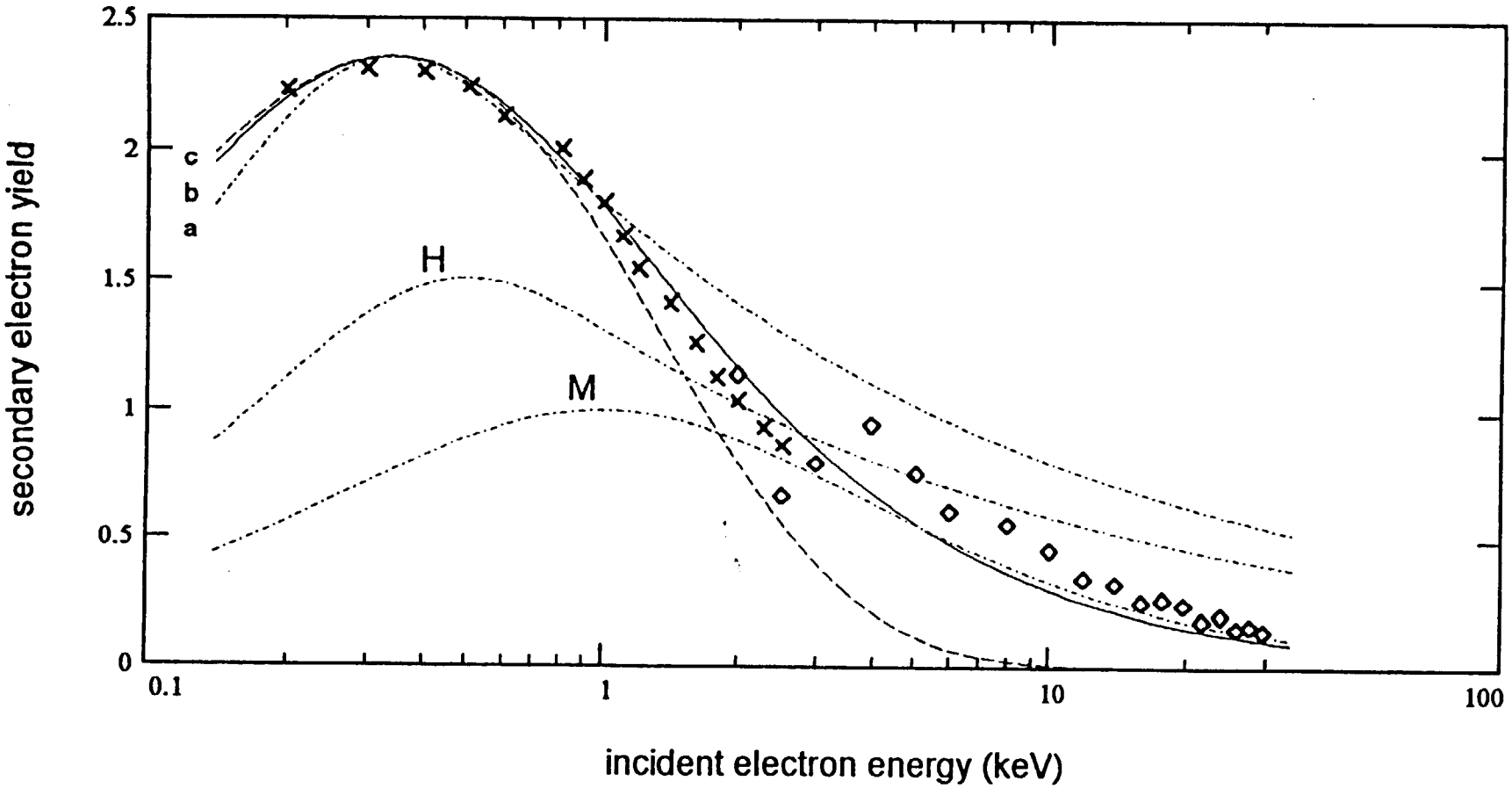
secondary electron yield
2.5
2
1.5
1
0.5
0
c
b
a
H
M
0.1
1
10
100
incident electron energy (keV)

Figure 2

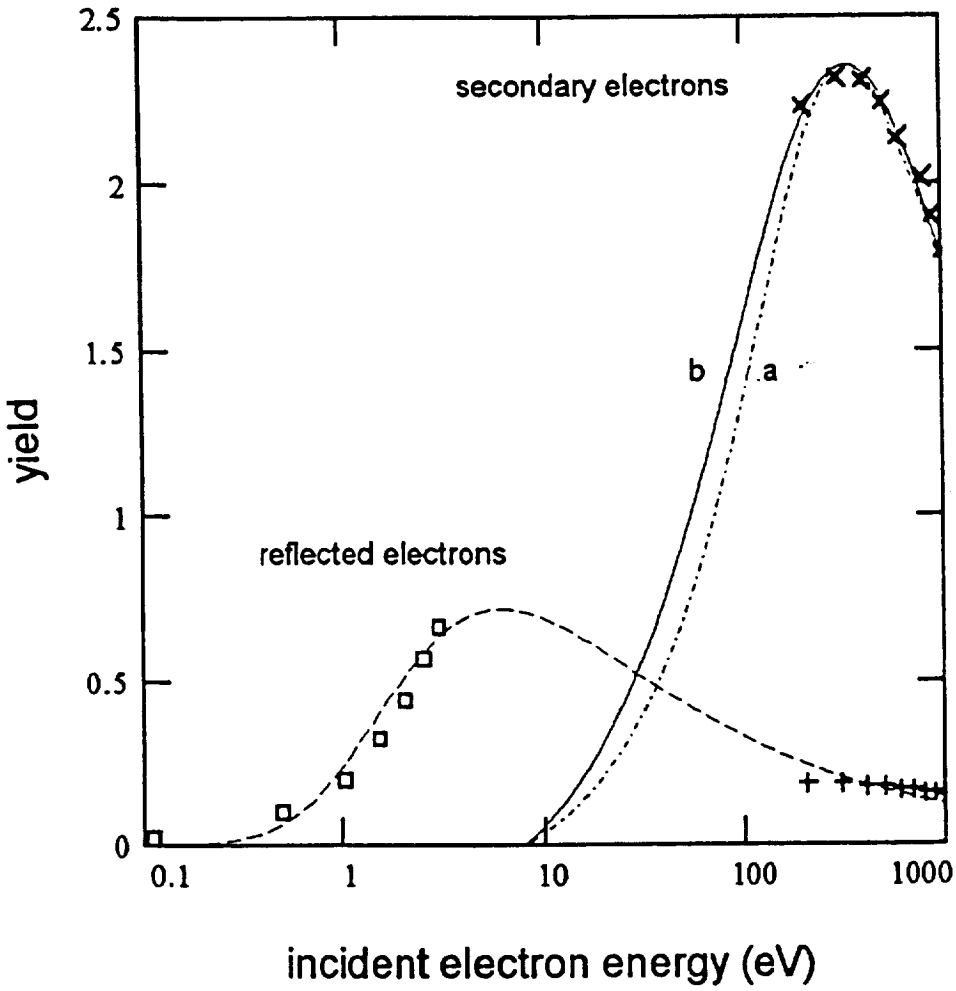
2.5
2
1.5
1
0.5
0
yield
secondary electrons
b
a
reflected electrons
0.1
1
10
100
1000
incident electron energy (eV)

Figure 3

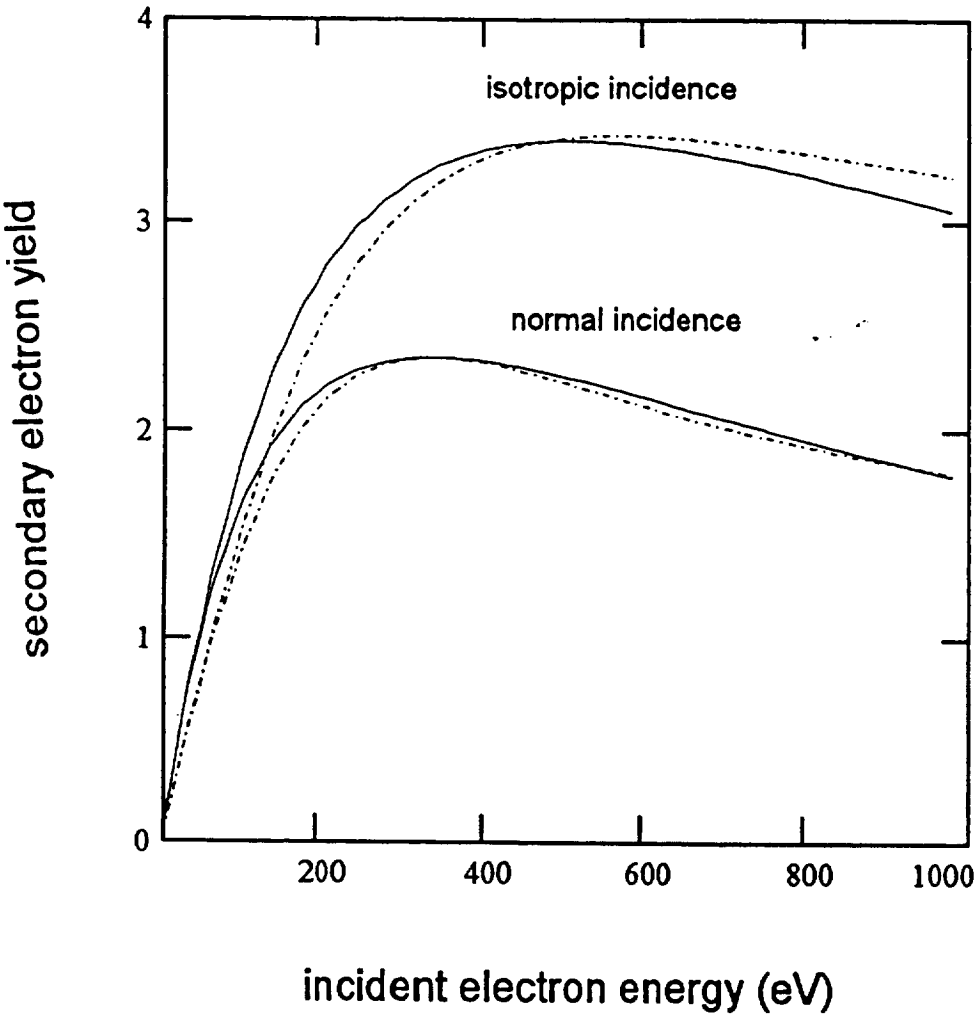
4
3
2
1
0
isotropic incidence
normal incidence
200
400
600
800
1000
secondary electron yield
incident electron energy (eV)

Figure 4

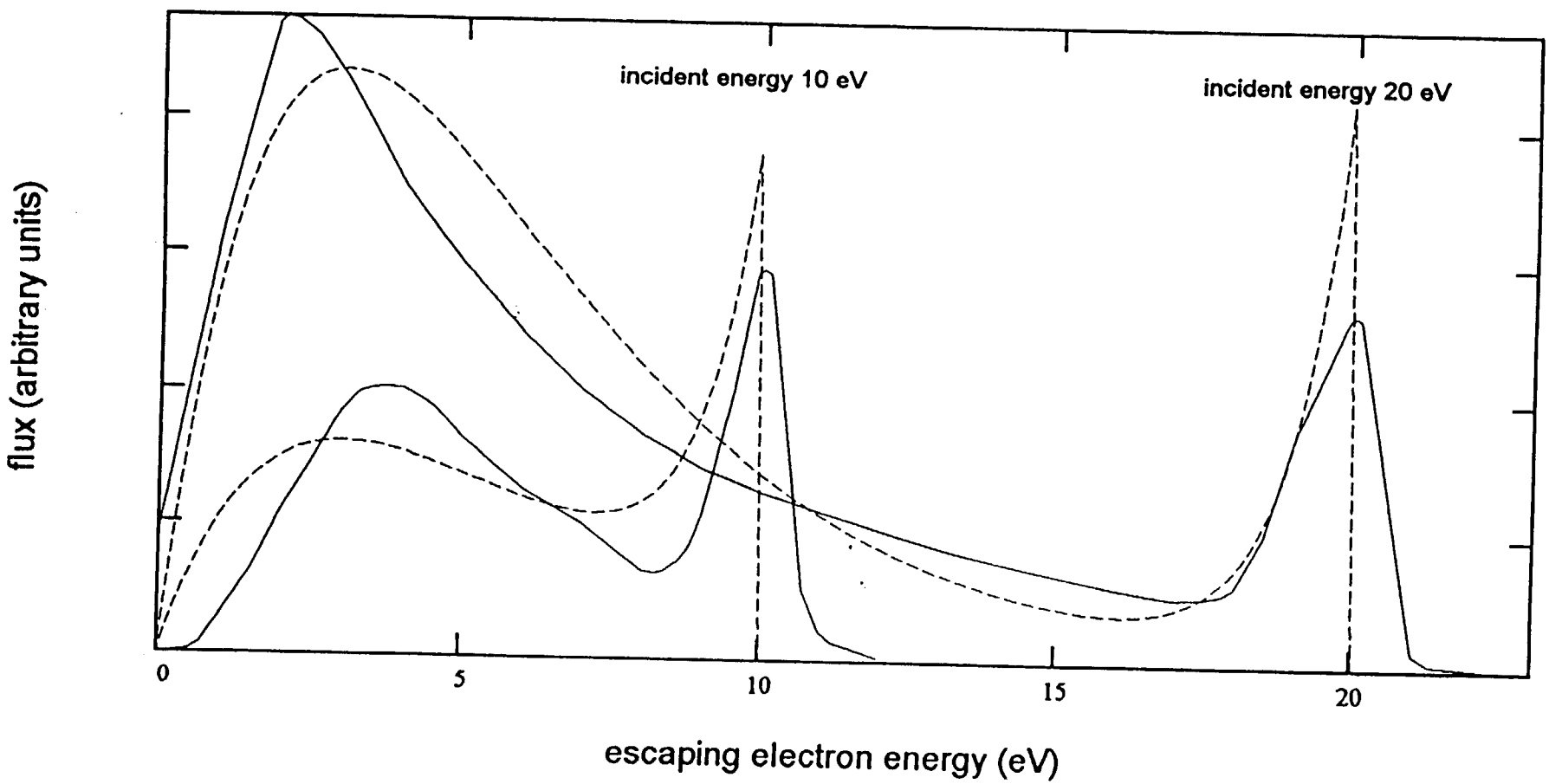
incident energy 10 eV
incident energy 20 eV
flux (arbitrary units)
0
5
10
15
20
escaping electron energy (eV)

Figure 5

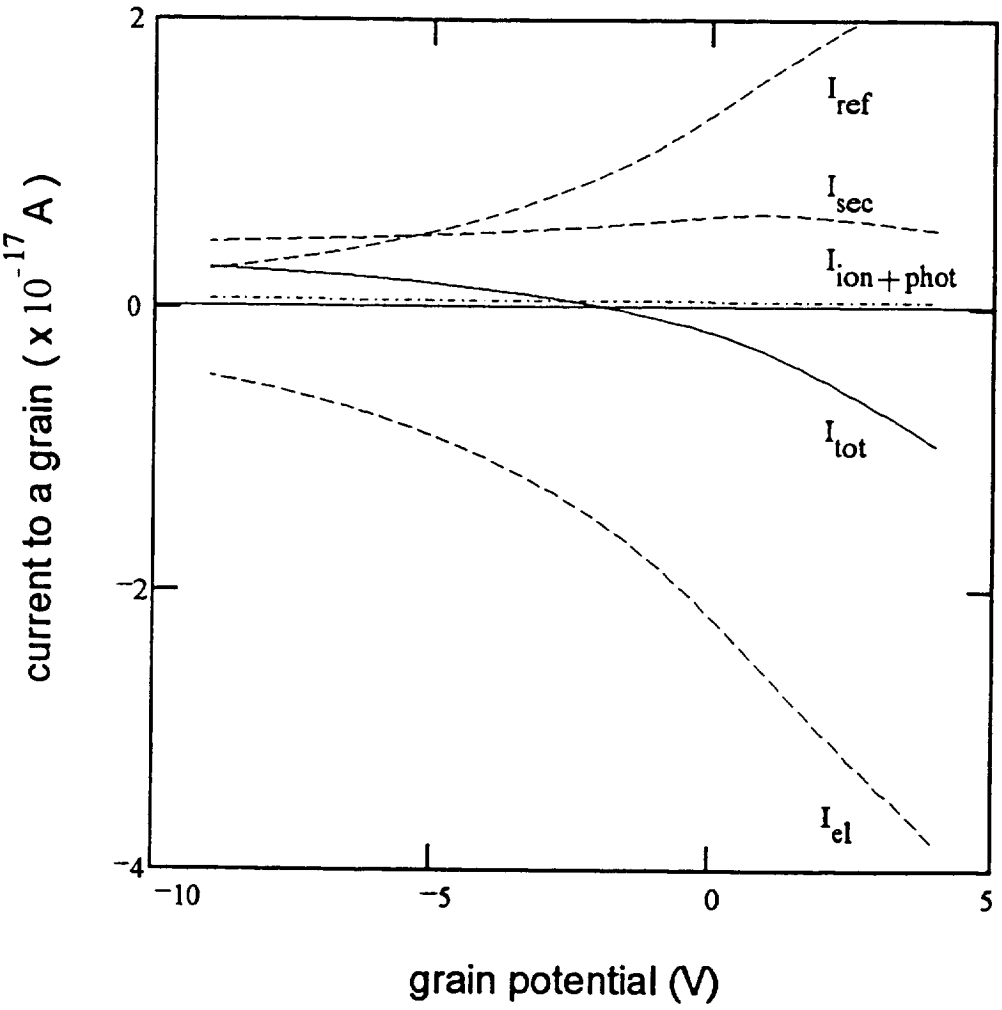
2
0
−2
−4
−10
−5
0
5
I_{ref}
I_{sec}
$I_{ion+phot}$
I_{tot}
I_{el}
current to a grain (x 10^{-17} A)
grain potential (V)

Figure 6

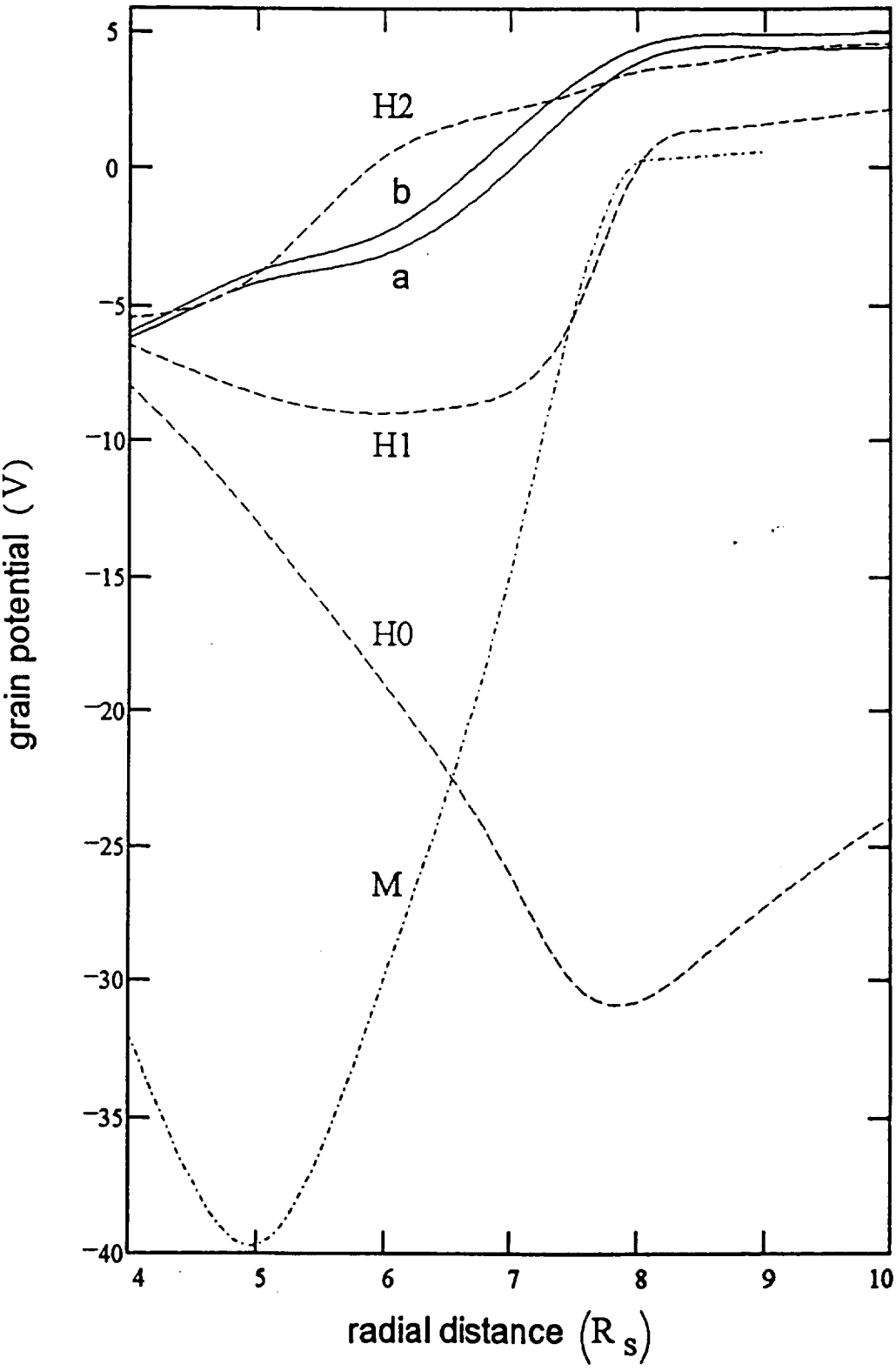
5
0
−5
−10
−15
−20
−25
−30
−35
−40
4
5
6
7
8
9
10
H2
b
a
H1
H0
M
grain potential (V)
radial distance (R s)

revised version

Particle Emission Induced by Ionization Tracks in Water Ice

M. Shi, D. E. Grosjean, J. Schou*, and R. A. Baragiola

Laboratory for Atomic and Surface Physics, Engineering Physics, University of Virginia, Charlottesville, VA 22901, USA

ABSTRACT

We study electron emission and sputtering during irradiation of amorphous water ice at 60 K by H^+, D^+, He^+, Li^+, Be^+, B^+, C^+, N^+, O^+, F^+, and Ne^+ ions in the energy range from 10 to 100 keV. We find that for constant velocity (5 keV/amu) ions the dependence of the sputtering yields with projectile atomic number Z is proportional to the square of the Z-dependence of the electronic stopping power dE/dx, using dE/dx values predicted by Yarlagadda, Robinson, and Brandt. The electron yields increase sublinearly with dE/dx, indicating the strong influence of un-neutralized holes in the ionization track produced by the projectiles.

*Permanent address: OFD, Risø National Laboratory, Denmark

1. INTRODUCTION

Fast ions moving through condensed matter produce a track of excitations and ionizations that can have lasting effects depending on the properties of the medium [1, 2, 3, 4]. A core of unbalanced holes results [5] from the fact that electrons receive almost all of the energy transfer which ejects them from the path of the ion. The central problem in describing the track is to understand the evolution of the electrons, holes, and excitations with time after the primary excitation events. In a metal the ionizations are screened very quickly by the free electrons (within 10^{-16}-10^{-15} s), whereas the ion core in an insulator may survive for much longer times ($>10^{-11}$ s). If the density of holes and liberated electrons is high, the behavior of the charged particles in the track becomes extremely complex, until neutralization eventually occurs.

The persistence of an unbalance of excess holes in the core of a track in insulators can damage the material through the action of the very large Coulomb repulsion between holes. This type of radiation damage is important in radiation biology, where it may cause the destruction of living cells [2,3]. In certain materials the damage tracks can be made visible and counted, and the information used in radiation dosimetry and in the dating of rocks [1].

The emission of particles (electrons, ions, neutral species) from the track of a projectile entering the insulator [6, 7, 8, 9] depends on ionization events that take place not only immediately below the surface, but further into the material as well. Because ejected electrons cannot return to the track to recombine with the holes, the effects of unbalanced Coulomb forces persist until the holes diffuse away (usually slowly) eventually reaching a conducting electrode where they neutralize.

The important process of ejection of electrons from insulators is not well understood due to uncertainties in the intervening physical mechanisms. Electrons may be excited into the conduction band by transitions from the valence band or core levels either produced directly by the projectile or through cascade multiplication of the excited electrons [10, 11] As is common to other ionization processes, the energy distribution of the excited electrons falls off very rapidly with electron energy [12]. Most of the excited electrons will have insufficient energy to excite other electrons across the band gap so they will lose energy slowly through excitation of atomic vibrations as they move away from the point of ionization. For *dilute* tracks, this motion will be mainly affected by the residual parent hole and by strong elastic scattering with atomic cores which tends to randomize the electron motion. Those electrons with a sufficiently large kinetic energy component perpendicular to the planar surface barrier (of magnitude equal to the electron affinity of the surface) will be ejected from the solid. The time between excitation and emission is expected to be small, of the order of a few fs, the value estimated for metals [13]. In this limit of dilute tracks, the number of emitted electrons is proportional to the number of electrons excited per unit path length, which is in turn proportional to the electronic stopping power of the projectile (dE/dx) at high velocities [10,11].

The termination of the track on the surface implies that the events which lead to radiation damage in the bulk of the solid can now eject atomic and ionic species, though most are neutral [14]. This form of sputtering can be much more important than elastic sputtering by direct momentum transfer by the projectile to lattice atoms, particularly for condensed gas solids [7]. Unlike elastic sputtering, where ejection occurs typically within a ps after the projectile hits the surface [15], electronic sputtering can occur over a much longer time scale ($> \mu s$). The energy

required for atomic motion does not necessarily come from Coulomb repulsion between holes (this process, in fact, has not yet been conclusively demonstrated) but from the decay of excitons into repulsive neutral states or, in molecular solids such as ices of water or carbon monoxide, from more complex processes involving radicals [16, 17, 18, 19].

The case of water ice is particularly interesting because of multiple applications. Among them are radiation biology, since amorphous ice is a good analog to liquid water, and astrophysics, where ices on cosmic grains and outer solar system objects are bombarded by ionizing radiation [19]. Brown et al. [17,20] have shown that ice can be sputtered readily by fast protons and found that the sputtering yield is proportional to the square of the electronic stopping power at MeV energies but deviates from this behavior for protons of tens of keV with similar values of electronic stopping power [20].

The energy release processes that lead to particle ejection during electronic sputtering of ice are not known in detail. Presumably, the ionizations and some of the higher-energy excitations initiate a sequence of processes from which one or several radicals are generated. When radicals from different ionization events react, some of the processes are sufficiently exothermic that intact molecules or fragments can be ejected [7, 19, 21, 22,].

In this work we present studies of the dependence of electron yields and sputtering on electronic stopping power for H^+, D^+, He^+, Li^+, Be^+, B^+, C^+, N^+, O^+, F^+, and Ne^+ ions in the energy range from 10 to 100 keV. We analyze the data in terms of the density of the ionization track.

2. EXPERIMENTAL

Experiments were performed in an ultrahigh vacuum chamber (Fig. 1) connected to a 120 keV ion accelerator. The base pressure in the chamber was $\sim 10^{-10}$ Torr , rising to $2 - 5 \times 10^{-9}$

Torr during the measurements. The rotatable target assembly is cooled by a closed-cycle refrigerator which can reach 20 K. A gold-coated quartz-crystal microbalance positioned at the target is used to measure the sputtering yields and film thickness. A second crystal mounted behind the target (not shown in fig. 1) is used in a heterodyne method as a reference to compensate the temperature dependence of the crystal frequency [23]. In this system, the areal mass sensitivity corresponds to about 0.1 monolayer of ice. Surrounding the target is an aluminum cylinder which acts as an anode for electron collection (when biased at +300 V) as well as a thermal shield against the heat from the chamber walls. Between the target and the anode is a 92% transparent nickel screen which is biased at -90 V from the anode to suppress secondary electron emission from the anode.

Amorphous ice films of 1200-1500 Å were grown by flowing vapor of outgassed high purity water through a capillary array doser onto the target crystal held at 60 K, then bombarded by 10-100 keV ions at normal incidence. The ranges of these ions in ice are all greater than the film thickness. Sputtering yields are determined by measuring the ion beam dose (typically ~10^{14} ions/cm^2) and the frequency change of the crystal. The electron yields (possibly including a very small fraction of negative ions) are determined by measuring the ion beam current to the target assembly and the electron current to the anode.

3. RESULTS AND DISCUSSION

3 A. Sputtering

The sputtering yield Y_S from water ice induced by 10-90 keV protons is shown in fig. 2. Sputtering induced by ion bombardment depends primarily on the binding energy of surface atoms

and the stopping power of the incident ion [7]. The dependence of the sputtering yield on the electronic stopping power is often analyzed in terms of a power law

$$Y_S = c(dE/dx)_e^n \qquad (1)$$

where c is a constant for a given material and n is determined empirically. The value of n is related to different physical processes: n=1 implies that sputtering results primarily from individual excitation or ionization events, while n=2 implies that excitations or ionizations interact to give rise to sputtering. Values in between and beyond indicate that varying degrees of interaction processes are responsible for sputtering. For our data in Fig. 2 we obtain $n = 1.3 \pm 0.2$, using the experimental dE/dx values of Bauer et al. [24] which we extrapolate below 30 keV.

In fig. 3 data for sputtering as a function of atomic number of the projectiles are presented together with the corresponding stopping powers, at a constant velocity corresponding to 5 keV/amu (9.8×10^7 cm/s). The square root of the sputtering yield as well as the stopping power have been normalized to the proton value. Since there are no measurements of stopping powers of ice for heavy projectiles, we use the Z-dependence of the stopping power given by Yarlagadda et al [25], which have been shown previously to describe accurately the Z-dependence of the electron yields from aluminum [26], valid in the limit of low velocities. The Z-dependence of stopping power $(dE/dx)_Z$ for slow ions at constant velocity is given by:

$$(dE/dx)_z = CZ^2\left[1-\exp(-0.95Z^{-2/3})\right]^2 \qquad (2)$$

which describes the overall trend but not the structure apparent in the experimental data of fig. 3 as Z goes from 5 to 6. We believe this structure is due to shell effects (Z-oscillations [26]) in the stopping power. Unlike the case of sputtering by protons of different energy, we see that changing dE/dx at constant velocity produces a quadratic dependence of the sputtering yield with

stopping power, as found for MeV protons. These two apparently inconsistent results can be reconciled by a velocity dependent c factor in Eq. (1).

3 B Electron Emission.

It is well known from the electron emission literature on metals that the electron yield is proportional to the stopping power [10, 26, 27, 28, 29]. This is a direct result of the fact that the electrons are dominantly produced by cascades rather than primary ionization alone [10, 30] which is proportional to the ionization cross section. Primary ionization alone is important for slow projectiles on insulators with a large band gap, like water ice. However, since the dependence of the stopping power [24] and the ionization cross section [31] with proton energies above 10 keV are fairly similar, and since the ionization cross section for other ions is not available, we will use the existing stopping power data.

The electron yields for protons increase with energy from about 1.7 electron/proton at 5 keV up to about 3 electrons/proton around 70 keV in the region of the maximum of dE/dx (fig. 2). The yields increase slower with energy than expected from the variation in the stopping power; we will return to that point below. The electron yield was found to be independent of the beam current density over an order of magnitude around the current densities used in these measurements (~ 0.2 $\mu A/cm^2$) , indicating that electron emission from these thin films is a single incident ion effect and does not involve macroscopic charging.

The electron yield for a number of ions incident on water ice with energy 5 keV/amu is shown in figs. 3 and 4 as a function of the atomic number of the projectile, Z. The yield increases towards a value around 3.6 electrons/ion for larger atomic numbers. The electron yield for a

number of ions incident on aluminum [26] is also shown in fig. 4 to compare to the case of metals. One notes that γ for aluminum is much lower than that from water ice for light projectiles, but that the ratio γ(ice)/γ(Al) decreases to a value around 1.4 for high Z. The lower electron emission for aluminum than for ice is consistent with the fact that metals generally have a low γ compared with insulators, but the strong decrease in the yield ratio suggests that an additional effect due to high ionization densities is acting in the insulator.

The Z-dependence of the electron yield from aluminum has been shown to be described very well by the stopping power expression from Yarlagadda et al. [25] mentioned above. Unlike the case of Al discussed by Alonso et al. [26], where there is a good agreement between the Z-dependence of the electron yields and the Z-dependence of the stopping power, for water ice, the $\gamma(Z)$ dependence lies far below the stopping power curve (fig.3). Therefore, one is led to the conclusion that electron emission from water is not just determined by the stopping power, but is strongly influenced by track processes. The decisive difference between Al and ice is that, unlike the case of Al, the ions in the track of ice are not screened during the electron ejection process. As indicated schematically in Fig. 5, the unbalanced holes in ice attract the electrons, preventing them from escaping, and, consequently, reduce the yield for a high hole density, i.e., a high stopping power. The magnitude of this effect caused by the unbalanced holes will be studied quantitatively in the following section on the basis of a simple model.

3 C. Model for Track Effects in Electron Emission

The electron yield from a metal can be well approximated by [10, 28]:

$$\gamma = B\,dE/dx \qquad (3)$$

B is a material dependent factor that takes into account the energy distribution of electrons in the solid and the transmission of electrons through the surface barrier:

$$B = \int_{U}^{\infty} f(E)T(E)dE \qquad (4)$$

As mentioned in the introduction, the internal energy distribution of excited electrons, $f(E)$, is a decreasing function of E, but the precise shape is not known for ice. We model it as $f(E) = b/E^2$ where b is a constant and assume that this functional form is independent of the track density. Since low energy electrons undergo strong elastic scattering inside the solid, they will arrive at the surface as an isotropic flux in the half space inside the solid. The probability of transmission through the planar surface barrier of magnitude U is given by [10]:

$$T(E) = \frac{1}{2}\left(1 - \sqrt{\frac{U}{E}}\right) \qquad (5)$$

The sub-linear increase of the electron yields with dE/dx observed here has been reported by Jacobsson and Holmén [32, 33] for ion bombarded SiO_2. These authors proposed that it is due in part to an additional barrier created by the space charge of the track. They fitted their data using an additional *planar* surface barrier to account for the space charge. We attempt here to calculate the average track potential acting on the escaping electrons. Furthermore, we assume that this potential will act similarly to a spherical barrier which is added to the planar barrier that the electron must overcome to escape. The spherical barrier is included by changing the limits of integration in Eq. (4) and by simply shifting the electron energy in the transmission function by U_S. Then:

$$B = b \int_{U+U_S}^{\infty} \frac{dE}{E^2}\left(1 - \sqrt{\frac{U}{E - U_S}}\right) \qquad (6)$$

The form of the transmission function accounts for both barriers: for $U_S = 0$ the transmission function is identical to the planar value (Eq. (5)), whereas for $U_s >> U$, it approaches the standard expression for a spherical barrier of height U_s. Integration yields

$$\gamma = \frac{b}{U_s}\left[1 - \sqrt{\frac{U}{U_s}}\left(\frac{\pi}{2} - \arctan\sqrt{\frac{U}{U_s}}\right)\right]\frac{dE}{dx} \qquad (7)$$

which tends to $\gamma = \frac{b}{U_s}\frac{dE}{dx}$ for large track potentials.

Calculation of an effective potential U_s is based on the assumption that the incident projectile produces a line of holes from the surface to the substrate separated by $W/(dE/dx)$ where W is the mean energy required to create an electron-hole pair (29 eV for water [34]). The potential is calculated at the surface by assuming that the number of unbalanced holes is equal to γ and that the potential is produced from the total charge placed at a depth $L/2$, where $L=\gamma W/(dE/dx)$. This leads to a potential U_S

$$U_s = \frac{2q^2}{4\pi\varepsilon}\frac{dE/dx}{W} \qquad (8)$$

where the dielectric constant $\varepsilon/\varepsilon_0 = 1.7$ [35], appropriate for energy transfers of eVs and tenths of eV. Using the density of 0.82 g/cm^3 for vapor deposited water ice [36] we obtain $U_S = 0.161(dE/dx)$ (eV/(10^{15}H$_2$O/cm^2)), which gives a track potential of ~9 eV for the highest stopping power used.

Figure 6 shows the results of plotting $\gamma = B(dE/dx)_e$ from eq. (7) with the data from figures 2 and 3. The stopping cross sections used for the proton data are from Bauer et al. [24] and those used for the other ions are obtained from the proton data using eq. (2). For these calculations we applied the potential U_S obtained from eq. (8) and the surface barrier was taken to

be $U = 0.9$ eV, equal to the electron affinity of water ice [37]. The curve was normalized to a value of 1.9 electrons/ion at 10 eV/($10^{15}H_2O/cm^2$). Even though the model is based on several simplifying assumptions, it describes well the trend of the data over the entire stopping power range. We believe that the structure suggested by the data of fig. 6 (as in fig. 3) is associated with Z-oscillations in dE/dx and in W [38].

5. CONCLUSIONS

Electronic sputtering and electron emission for keV ions incident on water ice are determined by the electronic stopping power and additional processes in the ionization track. The electronic sputtering yield grows linearly with the square of the electronic stopping power but the proportionality factor is velocity dependent for slow ions. The electron yield induced by light ions is larger for water ice than for metals, but the yield grows sub-linearly with electronic stopping power, due to the increase barrier produced by unbalanced holes in the insulator. A relatively simple model that includes a track potential acting as a spherical barrier can account for this effect.

ACKNOWLEDGEMENTS

This work was partially supported by NSF grant DMR-9121272. The authors thank W. L. Brown and R.E. Johnson for valuable discussions.

References

[1] R.L. Fleischer, P.B. Price, and R.M. Walker, Nuclear Tracks in Solids, Univ. of Calif. Press, Berkeley (1975).

[2] W. Brandt and R. H. Ritchie, in: Physical Mechanisms in Radiation Biology, eds. R.D. Cooper and R.W. Wood (US Atomic Energy Commission, Washington 1974) 20.

[3] R.H. Ritchie, R.N. Hamm, J.E. Turner, H.A. Wright, J.C. Ashley and G.J. Basbas, Nucl. Tracks Radiat. Meas. 16 (1989) 141.

[4] R.E. Johnson, in: Ionization of Solids by Heavy Particles, ed. R.A. Baragiola (Plenum, New York, 1993) 419.

[5] G. Schiwietz, et al., Phys. Rev. Lett. 69 (1992) 628.

[6] R.H. Ritchie and C. Claussen, Nucl. Instr. Meth. 198 (1982) 133.

[7] R.E. Johnson and J. Schou, Mat. Fys. Medd. Dan. Vid. Selsk. 43 (1993) 403.

[8] T.A. Tombrello, Nucl. Instr. and Meth.. B 2 (1984) 555.

[9] H. Rothard, Scan. Micr. To be published.

[10] R.A. Baragiola, Nucl. Instr. Meth. B 78 (1993) 223.

[11] J. Schou, in: Ionization of Solids by Heavy Particles, ed. R.A. Baragiola (Plenum, New York 1993) 351.

[12] M.E. Rudd, Y.-K Kim, D.H. Madison and T.J. Gay, Rev. Mod. Phys. 64 (1992) 441.

[13] A. Dubus, J. Devooght and J.C. Dehaes, Phys. Rev. B 36 (1987) 5510.

[14] K. Wien, Rad. Eff. Def. Solids 109 (1989) 137.

[15] N.Q. Lam, Scan. Micr. Suppl. 4 (1990) 311.

[16] W.L. Brown, W.M. Augustyniak, K.J. Marcantonio, E.H. Simmons, J.W. Boring, R.E. Johnson and C.T. Reimann, Nucl. Instr. Meth. B 1 (1984) 307.

[17] W.L. Brown and R.E. Johnson, Nucl. Instr. Meth. B 13 (1986) 295.

[18] D.B. Chrisey, W.L. Brown and J.W. Boring, Surf. Sci. 225 (1990) 130.

[19] M. S. Westley, R. A. Baragiola, R. E. Johnson and G. Baratta, Nature (in press).

[20] W. L. Brown, W. M. Augustyniak, E. Brody, B. Cooper, L. J. Lanzerotti, A. Ramirez, R. Evatt and R.E. Johnson, Nucl. Instr. Meth. 170 (1980) 321.

[21] R.E. Johnson, Energetic Charged Particle Interactions with Atmospheres and Surfaces, Springer-Verlag, Berlin (1990).

[22] R.L. Hudson and M.H. Moore, J. Phys. Chem. 96 (1992) 6500.

[23] N. J. Sack and R.A. Baragiola, Phys. Rev. B 48 (1993) 9973.

[24] P. Bauer, W. Käferböck and V. Necas, Nucl. Instr. Meth. B 93 (1994) 132.

[25] B.S. Yarlagadda, J.E. Robinson and W. Brandt, Phys. Rev. B 17 (1978) 3473.

[26] E.V. Alonso, R.A. Baragiola, J. Ferrón, M.M. Jakas, and A. Oliva-Florio, Phys. Rev. B 22 (1980) 21.

[27] J. Schou, Scan. Micr. 2 (1988) 607.

[28] D. Hasselkamp, Springer Tracts Mod. Phys. 123 (1992) 1.

[29] R.A. Baragiola, in: Low Energy Ion-Surface Interactions, ed. J.W. Rabalais (John Wiley, 1994) 187.

[30] P. Sigmund and S. Tougaard, in: Inelastic Particle-Surface Collisions, ed. E. Taglauer and Heiland, Springer Ser. Chem. Phys. 17 (1981) 2.

[31] M.E. Rudd, T.V. Goffe, R. DuBois and L. H. Toburen, Phys. Rev. A 31 (1985) 492.

[32] H. Jacobsson and G. Holmén, J. Appl. Phys. 74 (1993) 6397.

[33] H. Jacobsson and G. Holmén, Phys. Rev. B 49 (1994) 1789.
[34] Average Energy Required to Produce an Ion Pair, International Commission on Radiation Units and Measurements Report (1979) 31.
[35] S. G. Warren, Appl. Optics 23 (1984) 1206.
[36] M.S. Westley, MSc. Thesis (University of Virginia, 1994).
[37] B. Baron, D. Hoover and F. Williams, J. Chem. Phys. 68 (1978) 1997.
[38] J.R. MacDonald and G. Sidenius, Phys. Lett. A 28 (1969) 543.

FIGURE CAPTIONS

Fig. 1. UHV experimental apparatus. The polarity of the 300 V battery is reversed to measure sputter yields.

Fig. 2. Sputtering and electron yields of H_2O ice films vs. proton energy. The hollow circle and filled triangle are 10-keV D^+ points. The squares are sputter yields from Brown et al. [20]. Only some representative relative error bars are shown, while the lines are to guide the eye.

Fig. 3. Electron yields and sputter yields from water ice as a function of the atomic number Z normalized to the proton yield; stopping power from Yarlagadda et al. [25] normalized to the proton stopping power.

Fig. 4. Electron yields from Al and water ice vs. projectile atomic number (Z) at 5 keV/amu. Circles are yields from H_2O ice films (this work), triangles are yields from Al (extrapolated from Alonso et al. [26]).

Fig. 5. The model for unbalanced holes forming an effective potential in a track. Outgoing electrons (●) are attracted by the unbalanced holes (⊕), which act to produce an additional barrier.

Fig. 6. Electron yield as a function of the electronic stopping cross section. The line is calculated using the model of Sec. 3C and is normalized to 1.9 electrons/ion at 10 eV/($10^{15}H_2O/cm^2$). The experimental data is from the present work (proton data from fig. 2 and other ion data from fig. 4).

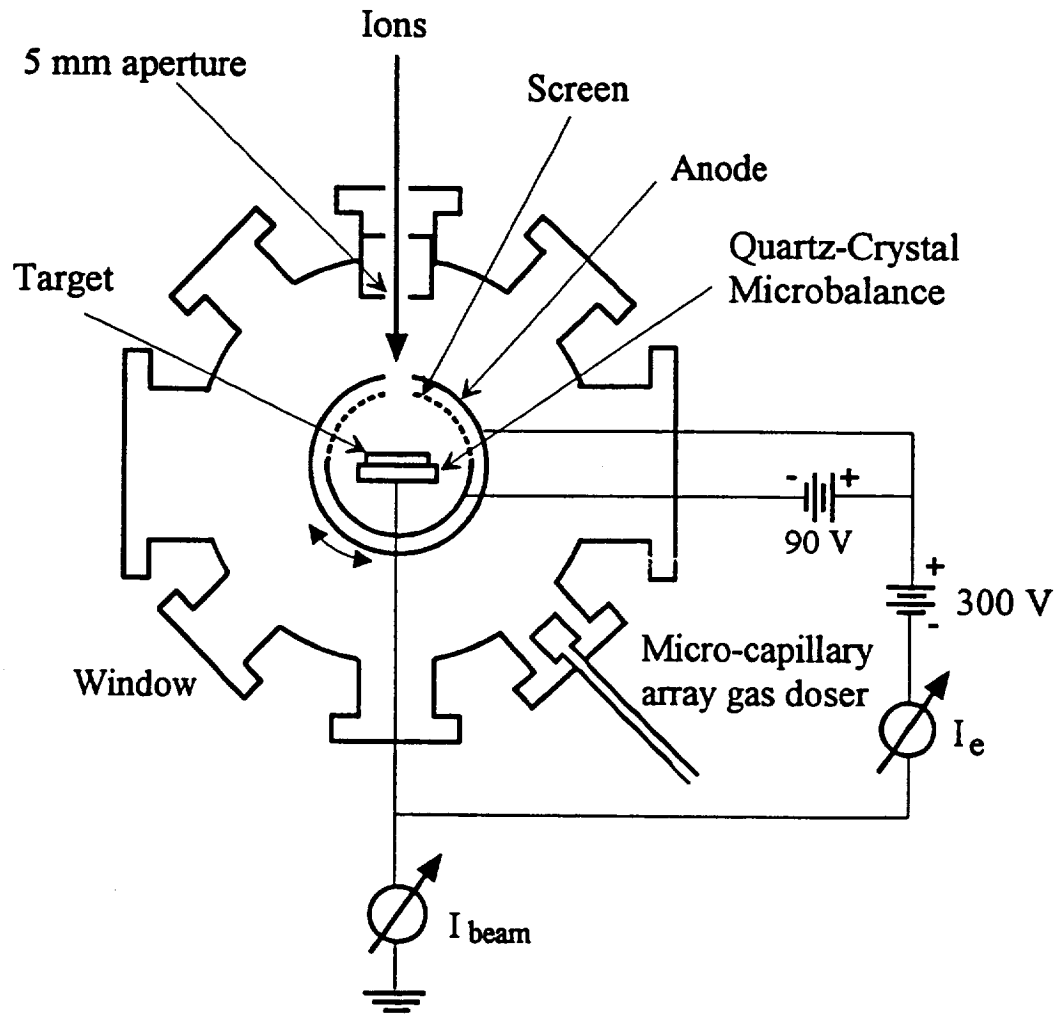
Ions
5 mm aperture
Screen
Anode
Quartz-Crystal
Microbalance
Target
-
+
90 V
+
300 V
-
Micro-capillary
array gas doser
Window
I_e
I_{beam}

Fig. 1.

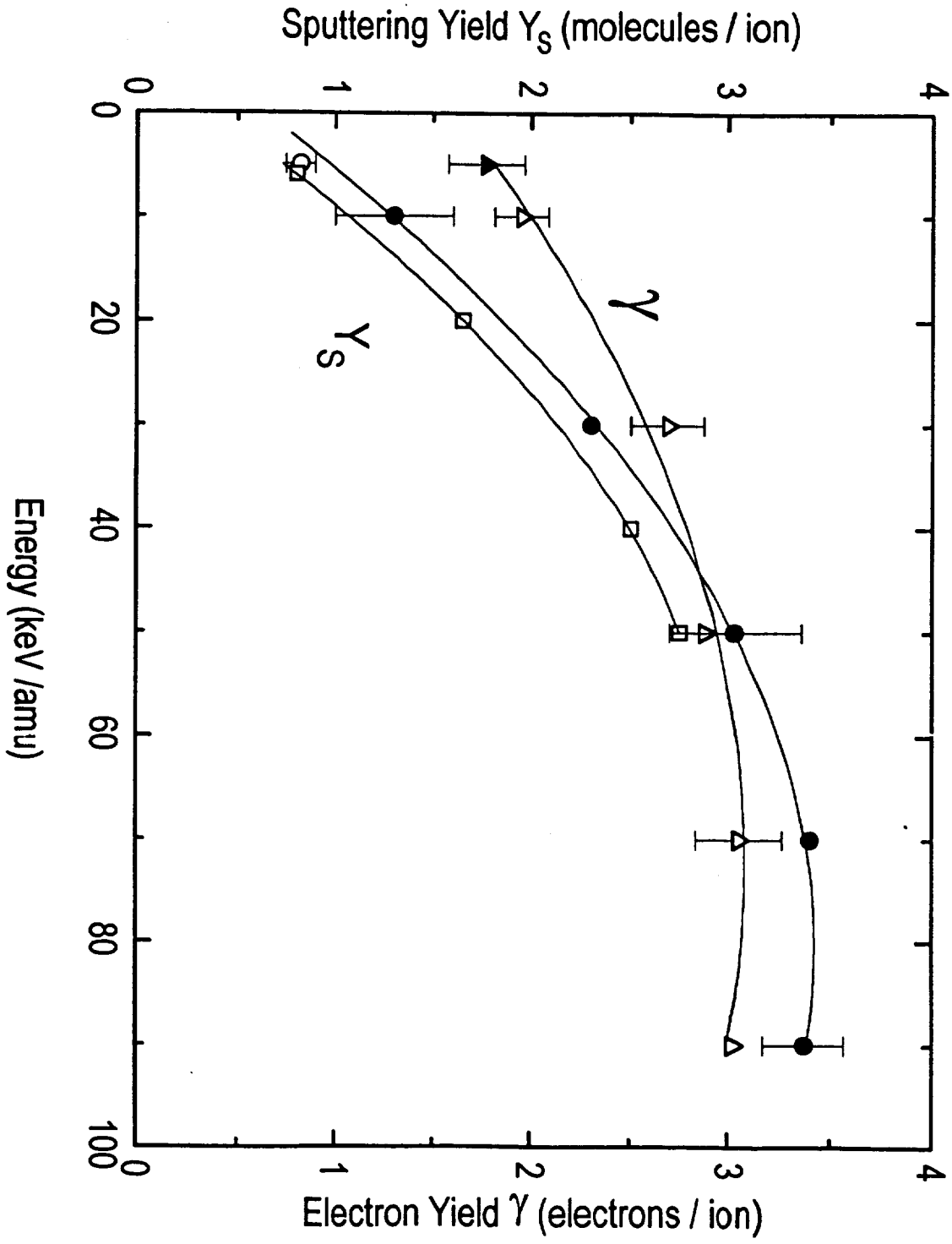
Sputtering Yield Y_S (molecules / ion)
Energy (keV /amu)
Electron Yield γ (electrons / ion)
γ
Y_S
0
20
40
60
80
100
1
2
3
4

Fig. 2.

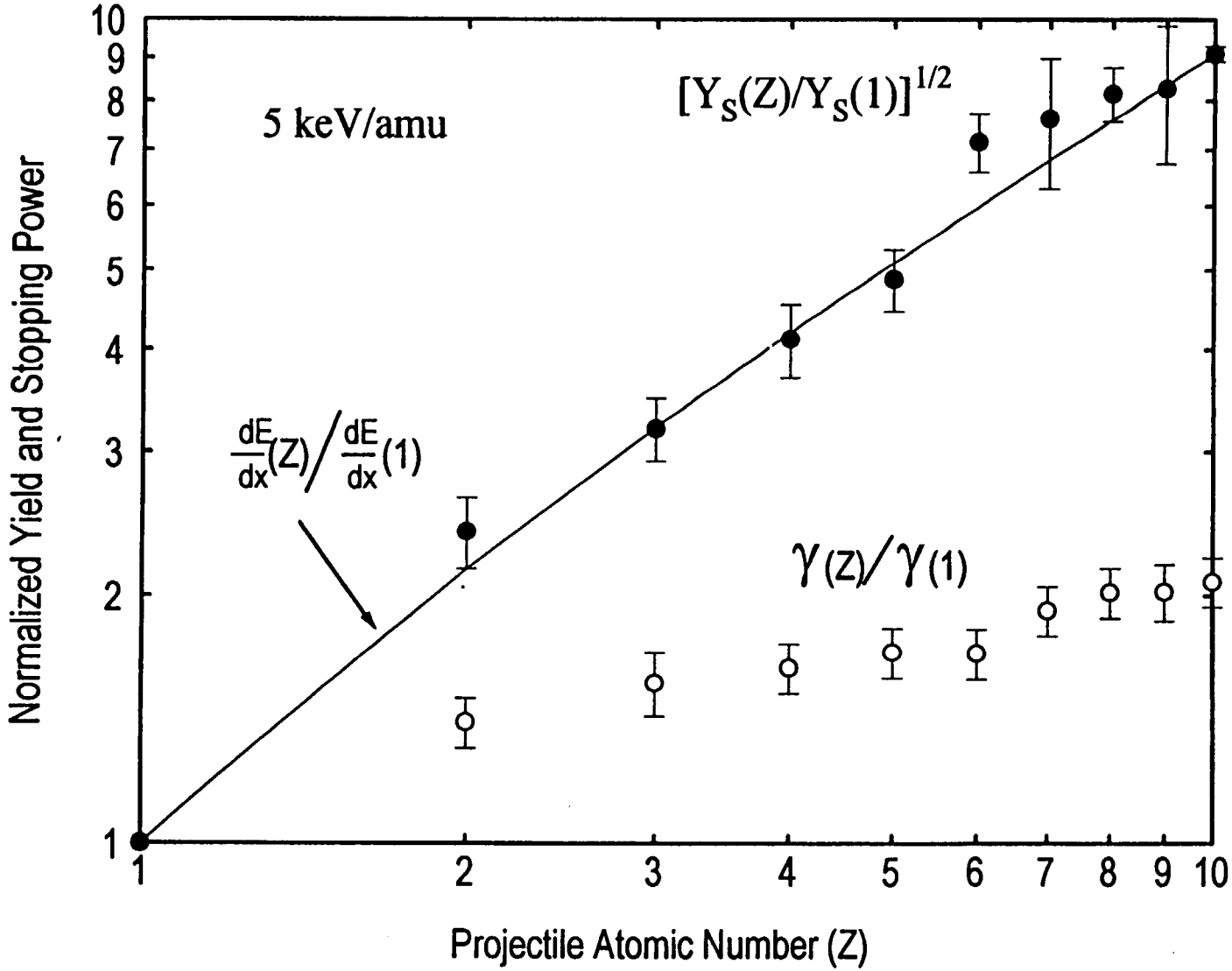
5 keV/amu
$[Y_S(Z)/Y_S(1)]^{1/2}$
$\frac{dE}{dx}(Z)/\frac{dE}{dx}(1)$
$\gamma(Z)/\gamma(1)$
Normalized Yield and Stopping Power
Projectile Atomic Number (Z)
1
2
3
4
5
6
7
8
9
10

Fig. 3.

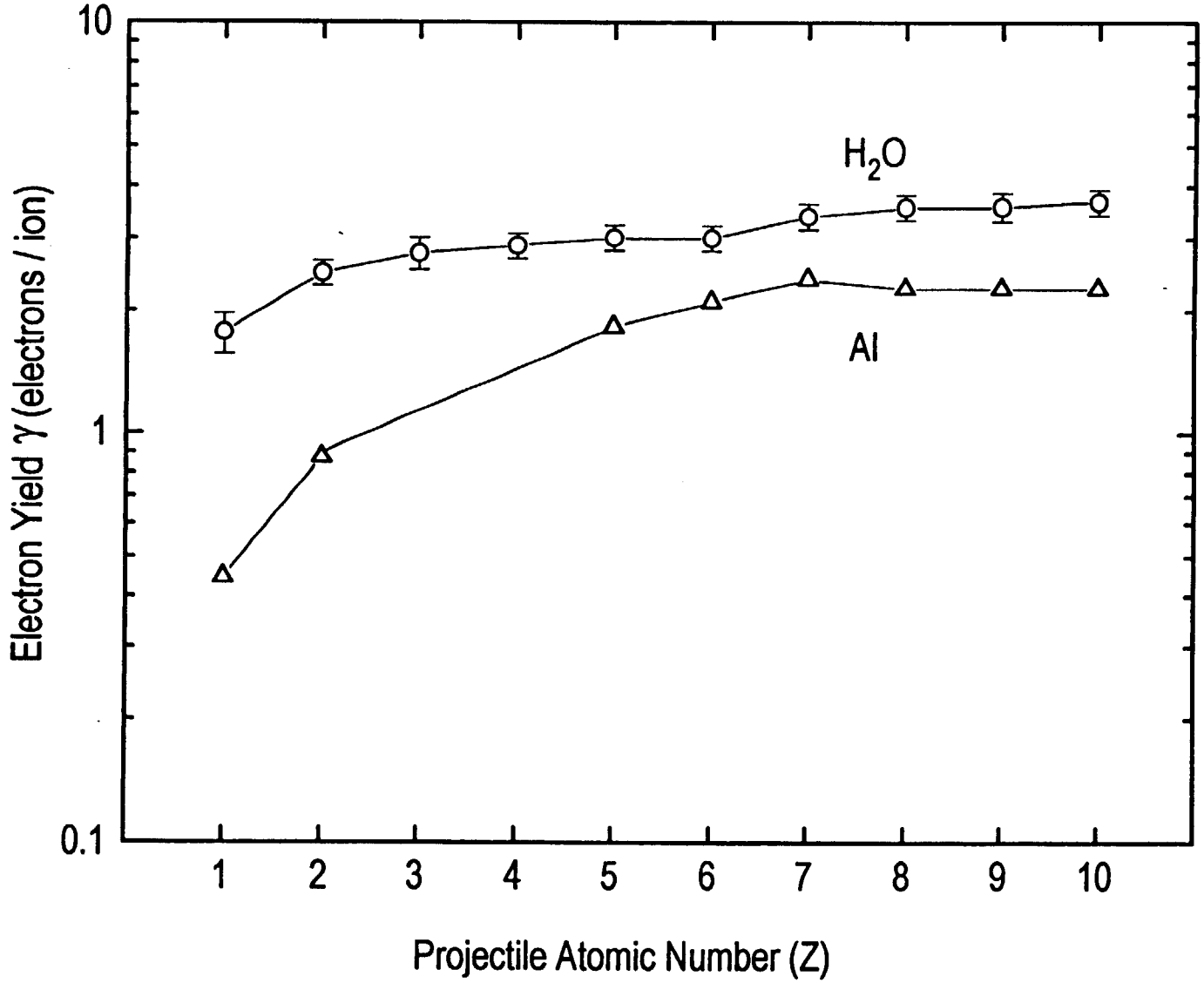
10
1
0.1
Electron Yield γ (electrons / ion)
H_2O
Al
1
2
3
4
5
6
7
8
9
10
Projectile Atomic Number (Z)

Fig. 4

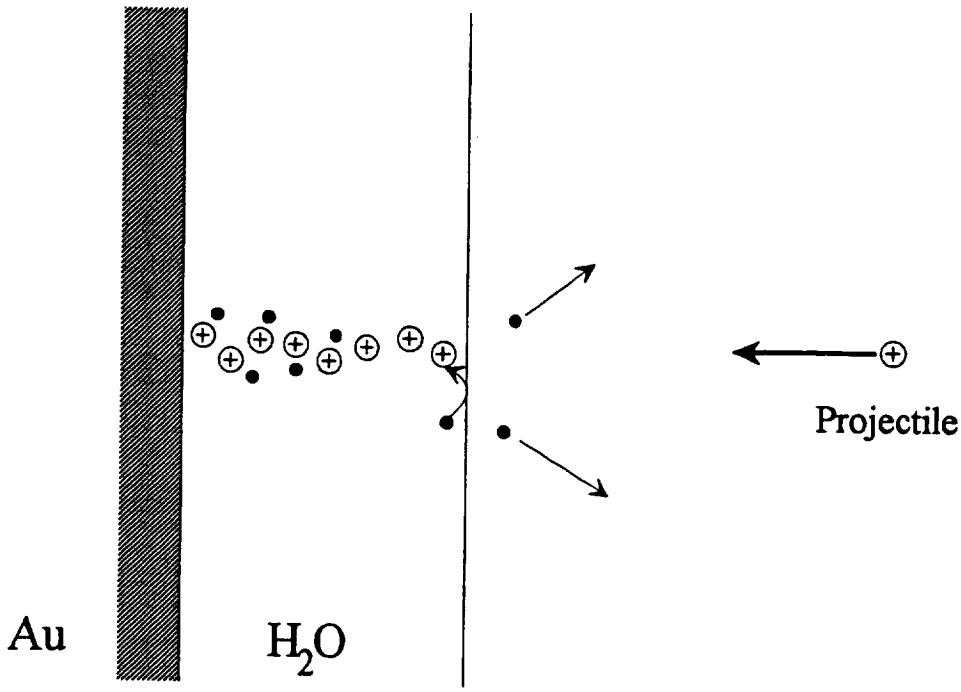

Fig. 5.

ORIGINAL PAGE IS
OF POOR QUALITY

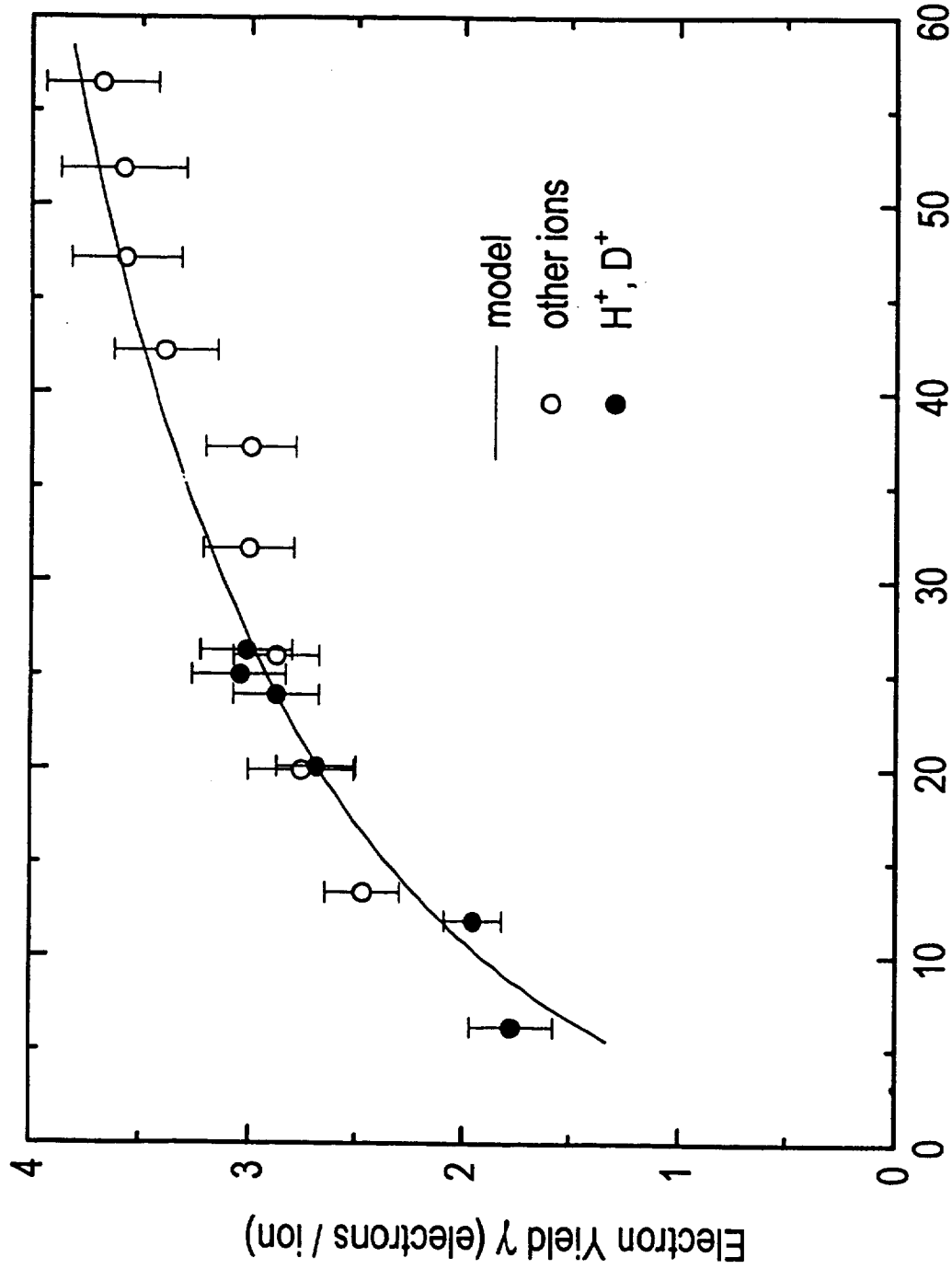

Fig. 6

DISTRIBUTION LIST

1 - 3	Robert Hoffman, Discipline Scientist Magnetospheric Physics Branch Space Physics Division Code SS National Aeronautics and Space Administration/Headquarters 300 E Street, S. W. Washington, DC 20546
4	Ms. Dean Yoshioka National Aeronautics and Space Administration/Headquarters 300 E Street, S. W. Washington, DC 20546
5 - 6*	NASA Scientific and Technical Information Facility P. O. Box 8757 Baltimore/Washington International Airport Baltimore, MD 21240
7 - 8	H. Earnhardt, Clark Hall
9 - 10	R. A. Baragiola
11	W. A. Jesser
**	SEAS Postaward Research Administration
12	SEAS Preaward Research Administration

*1 Reproducible copy
**Copy of cover letter

JO#6202:ph

ORIGINAL PAGE IS
OF POOR QUALITY